Adduct-based p-doping of Organic Semiconductors

Nobuya Sakai[1], Ross Warren[1], Fengyu Zhang[2], Simantini Nayak[3,4], Junliang Liu[5], Sameer V. Kesava[1], Yen-Hung Lin[1], Himansu S. Biswal[6], Xin Lin[2], Chris Grovenor[5], Tadas Malinauskas[7], Aniruddha Basu[8], Thomas D. Anthopoulos[8],Vytautas Getautis[7], Antoine Kahn[2], Moritz Riede[1], Pabitra K. Nayak*[1,9] and Henry J. Snaith*[1]

[1] Clarendon Laboratory, Department of Physics, University of Oxford, Parks Road, Oxford OX1 3PU, UK
[2] Department of Electrical and Computer Engineering, Princeton University, Princeton, New Jersey 08544, United States
[3] Department of Chemistry, University of Oxford, Inorganic Chemistry Laboratory, South Parks Road, Oxford OX1 3QR, UK
[4] Materials Chemistry Department, CSIR-Institute of Mineral and Materials Technology, Bhubaneswar, 751013, India
[5] Department of Materials, University of Oxford, Parks Road, Oxford OX1 3PH, UK
[6] School of Chemical Sciences, National Institute of Science Education and Research, 752050 Bhubaneswar, India
[7] Department of Organic Chemistry, Kaunas University of Technology, Radvilenu pl. 19, Kaunas LT-50254, Lithuania
[8] King Abdullah University of Science and Technology (KAUST), KAUST Solar Center (KSC), 23955-6900, Thuwal, Kingdom of Saudi Arabia
[9] TIFR Centre for Interdisciplinary Sciences, Tata Institute of Fundamental Research,
Hyderabad, 500046, India
Email: pabitra.nayak@tifrh.res.in; henry.snaith@physics.ox.ac.uk

Characterization

Conductivity measurement: For Figure 1c, 1d, Supplementary Figure 6, and 22, HTM solutions with various amounts of dopant were spin coated at 2000 rpm onto glass slides and were dried at 50 °C for 10 minutes in inert atmosphere. The HTM film thickness was 70-100 nm. Au contacts (~80 nm thick) were prepared via vacuum (5×10^{-6} Torr) thermal evaporation through a shadow mask. The electrode pattern was designed for four-point probe measurements with a force channel length (direction of current flow) of 1 mm and a width of 1 cm and a sense channel length of 300 μm and width of 1 mm. The current-voltage characteristics of these samples were collected at room temperature with a Keithley 2420 source meter unit to extract both the bulk and the contact resistance. For Figure 3b, 3c, Supplementary Figure 4 and 5, organic field-effect transistor (OFET) chips from Fraunhofer IPMS (Dresden, Germany) with bottom-gate and bottom-contact geometry were used. The gate oxide was 90 nm thick on top of an n-doped Si wafer. The 30 nm gold/ITO interdigitated fingers of the source and drain contacts had varying channel lengths of 2.5 μm, 5 μm, 10 μm and 20 μm. HTM solutions were spin coated at 2000 rpm onto the OFET chips and were dried at 50 °C for 10 minutes in inert atmosphere. The HTM film thickness was 70-100 nm. Under ambient conditions, a Keithley 2400 source measurement unit was used to perform current-voltage measurements across the varying channel lengths with no applied bias at the gate.

Kelvin probe measurement: Samples for the Kelvin probe measurement were prepared on F-doped tin oxide (FTO) glass substrate by a spin coating method. A Kelvin probe setup (probe diameter = 2 mm, KP Technology, UK) was used to measure the surface potential. Calibration of the Kelvin probe was done by a freshly cleaved highly ordered pyrolytic graphite surface which has known work function of 4.65 eV.[1] The measurements were done in ambient.

UPS and XPS measurement: UPS and XPS measurements were carried out in an ultra-high vacuum (UHV) chamber with a base pressure of $<2 \times 10^{-10}$ Torr. Samples were prepared in nitrogen and transferred under nitrogen directly to UHV without air exposure. UPS was performed with both the He I (21.22 eV) and He II (40.81 eV) photon lines. For each UPS spectrum, the satellite lines of the He discharge lamp were carefully subtracted. The vacuum level was determined from the low-energy secondary-electron cutoff seen in the UPS He I spectra. XPS was performed with non-monochromatized Al Kα X-rays (1486.70 eV), and Origin Lab Pro was used for XPS peak fitting. A double-pass cylindrical mirror analyzer was used to measure the kinetic energy of electrons from UPS He I, UPS He II and XPS with an overall measurement resolution of 0.15 eV, 0.25 eV and 0.80 eV, respectively. The Fermi level reference for both UPS and XPS were determined with a clean Au substrate in electrical contact with the sample. Sample measurements were kept as short as possible to avoid degradation of the organic materials.

Morphological characterization: A scanning electron microscope (SEM; Hitachi, S-4300) was used to acquire SEM images. The thickness of hole-transporting layers was measured by a stylus surface profiler (Dektak 150 Veeco Instruments, Inc.)

Atomic force microscopy (AFM): Doped and undoped thin-films of MeO-TPD were prepared on Si substrates. AFM measurements were performed on Bruker Innova AFM system. Silicon cantilevers (TAP300-G) with a spring constant of 40 N m^{-1} and a resonance frequency of 300 kHz were used in tapping mode; data were further processed using Gwyddion.

UV-visible absorption spectroscopy: UV-vis absorption spectra were measured by a commercial spectrophotometer (Varian Cary 300 UV-Vis, USA). ~ 0.05 mg/ml of HTM in chlorobenzene or toluene was usually used for solution phase doping. ~100 nm of HTM thin films were deposited on glass substrates by spin coating and used for solid state measurements.

Attenuated total reflectance Fourier transform infrared spectroscopy (ATR-FTIR) measurement: Agilent FTIR spectrometer with liquid nitrogen cooled Mercury Cadmium Telluride (MCT) detector was used for in-situ IR spectroscopy. For multiple reflections of incident IR light a modified ATR accessory (GladiATR, PIKE Technologies) was placed inside the spectrometer.

A Si trapezoidal ATR reflection element with a dimension of 5 x 8 x 1 mm^3 and 39° angle of incidence at both short edges (Crystal GmbH, Germany) was used as the ATR crystal. The IR cell was developed in-house for in-situ experiments.[2] The Si crystal was attached to the baseplate of the IR cell with epoxy glue to prevent leakage in the cell.

For reaction mechanism study by ATR-IR: First, the spectrum of DMSO in chlorobenzene was recorded, then vapours of HBr (direct addition of HBr in H_2O solution was avoided to minimize the water content in the starting solution) allowed to interact with the DMSO in chlorobenzene solution and IR spectrum was recorded. Then a solution of Spiro-OMeTAD in chlorobenzene (70 mM) was added to the IR cell and IR spectrum was measured at different time intervals. IR data are presented as absorbance spectra with reference spectra collected at a bare Si ATR reflection element. Spectra were collected at a spectral resolution of 4 cm^{-1} and presented as 250 co-added scans.

For the detection of remnant DMSO/ DMSO:HBr adduct in the doped film by ATR-IR: 10 µL of adduct forming agent were added to 2.5 mL of Spiro-OMeTAD, 0.28 mM solution in chlorobenzene (Aldrich; anhydrous, ≥99.9%). The solution was mixed by a vortex mixer for 1 min and then kept for 20 mins at room temperature to prepare a heavily doped Spiro-OMeTAD solution. 100 µL of the doped Spiro-OMeTAD was drop cast on a Si ATR crystal and the film was allowed to dry by keeping the ATR crystal at 40 °C on a hot plate. The ATR crystal then brought to the room temperature and FTIR spectrum of the film recorded.

Gas chromatography–mass spectrometry (GC-MS) measurement: Adduct forming agent was added to Spiro-OMeTAD solution (0.28 mM) in chlorobenzene and the gaseous by-products from the solution was analyzed using a GC MS (Agilent Technologies 6890N Gas Chromatograph with an Agilent 5973 Mass Selective Detector and a 50QC2/BPI column from SGE Ltd) set up.

High-resolution secondary ion mass spectrometry characterization: Asymmetrically doped ~300 nm Poly-TPD films were deposited onto Si substrates (see Methods for the preparation of thin-film). Localization of sulfur in these samples was investigated by high-resolution secondary ion mass spectrometry (SIMS) by performing elemental mapping in a CAMECA NanoSIMS 50 system using a focused 16 keV Cs^+ primary beam. The raster size was 2µm × 2 µm (16 × 16 pixels) and the dwell time was 4ms per pixel. Ion maps were collected simultaneously for $^{12}C^-$, $^{28}Si^-$, $^{32}S^-$ and $^{16}O_2^-$ ion signals, together with the secondary electron signal produced during the sputtering process, which can be used to show both sample morphology and surface topography. These scans were repeated 200 times from the same area, giving a set of stacked images of the distributions of each element, and sputtering to a total depth of ~300 nm below the sample surface. ImageJ with the OpenMIMS plugin[2] was used to read the raw SIMS data and create elemental depth profiles.

Ellipsometry measurement: 50 mg of N, N,N′,N′-Tetrakis(4-methoxyphenyl)benzidine (MeO-TPD) in chlorobenzene was stirred at 80 °C for 30 min. The DMSO-HBr or DMSO-HBr-CSA doped MeO-TPD solution was spin-coated onto a glass substrate at 2500 rpm for 45 sec (acceleration: 500 rpm). An undoped MeO-TPD film was deposited on top of the doped thin-film and also on bare glass substrates by thermal evaporation in vacuum (base pressure < 10^{-6} mbar). Ellipsometry measurements of the resulting films were carried out using an RC2 ellipsometer (J.A. Woollam). Ellipsometry measurements of the resulting films were carried out at 55, 65 and 75 degree. The optical constants derived from the undoped and undoped films were later used to analyze the ellipsometric profile of the stacked films. Measurements, analyses and simulation were done using Complete EASE software. The thermal tolerance test was carried out on a hot plate in ambient atmospheric conditions.

Mott- Schottky analysis: Mott-Schottky analysis on thick devices has been performed according to ref[3–7]. This analysis is based on the understanding that the depletion width at a semiconductor-metal contact changes with variation in the reverse bias potential. The measurements of the capacitance-voltage (C-V) scans were conducted typically between −5 V to 5 V with steps of 50 mV using an Autolab PGSTAT302F (Metrohm) at 1 kHz. During all

the measurements, the devices were kept in an inert atmosphere. The doping density N_A was obtained from the slope dC/dV of a C–V curve, following,

$$N_A = -\frac{2}{q\varepsilon A}\left(\frac{dC^{-2}}{dV}\right)^{-1} \quad \text{(SM1)}$$

where, $\varepsilon = \varepsilon_r\varepsilon_0$, ε_0 is the permittivity of free space, ε_r is the relative permittivity of the semiconductor ($\varepsilon_r \sim 3$),[6] A is the area and q is elementary charge.

The capacitance depends upon the change in space-charge region *w* controlled by the applied bias as following,

$$C = \frac{\varepsilon_0\varepsilon_r A}{w} \quad \text{(SM2)}$$

Therefore, for every point on the Mott-Shottky curve ($1/C^2$ vs V), we can calculate the N_A value from the slope, and the corresponding depletion width from Equation SM2.

Justification of which contact is being probed: FTO is always grounded and bias is applied to Au side irrespective of the doping interface in the device. The Capacitance-Voltage scans were done in both forward and reverse bias to probe the doped interface. As it can be seen in Supplementary Figure 29, due to the difference in the doping interfaces, the $1/C^2$ vs. V curve appear as mirror images of each other when the doping is at the FTO-PolyTPD, or poly-TPD-Au interface. This indicates that the contact being probed is the contact at the doped interface.

Thermal stability test: The thin films of hole-transporting materials were fabricated on top of a glass substrate for ellipsometry and on top of an OFET chip for the conductivity measurement. The thermal tolerance test was carried out on a hot plate in ambient atmospheric conditions for both of ellipsometry and conductivity measurements. For the thermal stress test, the substrates were heated at 50, 80 and100 °C for 10 min at each heating step. Measurements were done after heating at each temperature.

Characterization of PV devices: The current-voltage (J-V) measurements and stabilized power output (SPO) measurements were measured (2400 series source meter, Keithley Instruments) under both dark and simulated solar light (AAB ABET technologies Sun 2000 solar simulator) with its light intensity, 100 mW cm^{-2} (AM 1.5). The simulated light was calibrated against a standard amorphous-silicon PV cell (NREL-calibrated KG5 filtered silicon reference cell). The mismatch factor was estimated to be M=1.035405 and the lamp intensity was adjusted to account for this mismatch. The J-V curves were measured between 1.4V to 0V. The cell aperture area of light incidence was set to 0.0913 cm^2 by employing an opaque mask with an aperture.

Calculation of series resistance (R_s) *of the cell*:

The ideal fill factor of a solar cell in the absence of series resistance (R_s), FF_0 is given by[8]

$$FF_0 = \frac{\frac{qV_{OC}}{nkT} - ln\left(\frac{qV_{OC}}{nkT} + 0.72\right)}{\frac{qV_{OC}}{nkT}} \quad \text{(SM3)}$$

Where, V_{OC} is the open circuit voltage of the solar cell, q is the electronic charge, k is the Boltzmann's constant, T is the temperature of the cell and n is the ideality factor.

An empirical expression for the fill factor with series resistance, FF_S is given by[8]

$$FF_s = FF_0(1 - r_s) \quad \text{(SM4)}$$

Where r_s is the normalized resistance of the cell and given by

$r_s = \frac{R_s \times I_{SC}}{V_{OC}}$ (SM4)

Where I_{SC} is the short circuit current of the cell and R_s is the series resistance.

The FF_0 value for a solar cell was calculated using the measured qV_{OC} of the cell and taking *n* value as 1 and T = 298K

Then r_s value for the cell was calculated using the measured fill factor (FF_s) and FF_0

Rearrangement of SM4 gives the expression for the series resistance (R_s) as

$R_s = \frac{r_s \times I_{SC}}{V_{OC}}$ (SM5)

The R_s value of the cell was calculated using SM5.

External quantum efficiency (EQE) measurement: EQE spectra were evaluated via custom-built Fourier transform photocurrent spectroscopy based on the Bruker Vertex 80v Fourier transform spectrometer. A Newport AAA sun simulator was used as the light source and the light intensity was calibrated with a Newport-calibrated reference silicon photodiode.

Characterization of OLED: The current density-voltage (*J-V*) measurements were measured using a source meter (2400 series source meter, Keithley Instruments). The luminescence intensity was measured along with bias voltage from source meter, and luminescence was collected using with a fiber-coupled detector (Ocean Optics USB 2000+) in an integrating sphere (Oriel Instruments 70682NS).

Quantum Chemical calculation: The geometry optimization and normal mode vibrational frequency calculations of DMSO, DMSO:HX and DMSO:2HX (where X= Cl, Br or I) were performed at M06-2X/aug-cc-pVDZ level. The optimized structures are the energy minimum structures as verified with all positive vibrational frequencies. The Gaussian 09 software was used for the calculations.

Supplementary Table 1 | Ionization energy (IE) of hole-transporting materials (HTM) and the conductivity of HTM thin films before and after doping via vapor phase (exposure time 30 seconds) Organic field-effect transistor (OFET) chips from Fraunhofer IPMS (Dresden, Germany) with bottom-gate and bottom-contact geometry are used to fabricate the samples.

Organic semiconductor	Ionization Energy (IE) [ref.] (eV)	σ ($\times 10^{-6}$ S cm^{-2}) Before doping	σ ($\times 10^{-6}$ S cm^{-2}) After doping
N2,N2,N2′,N2′,N7,N7,N7′,N7′-octakis(4-methoxyphenyl)-9,9′-spirobi[9H-fluorene]-2,2′,7,7′-tetramine (Spiro-OMeTAD)	~5.0[9,10]	0.04 ± 0.01	29.1 ± 10.6
1,2-Bis[3,6-(4,4`-dimethoxydiphenylamino)-9H-carbazol-9-methyl]benzene (V886)	5.04[11]	0.03 ± 0.01	112 ± 30.3
N,N,N′,N′-Tetrakis(4-methoxyphenyl)benzi-dine (MeO-TPD)	4.97~ 5.1[12–14]	0.07 ± 0.01	3.83 ± 0.27
Poly(3-hexylthiophene-2,5-diyl) (P3HT)	5.0[15,16]	61.7 ± 2.90	$1.32\times10^{5} \pm 4.83\times10^{3}$
Poly[bis(4-phenyl)(2,4,6-trime-thylphenyl)amine] (PTAA)	5.2[17,18]	0.04± 0.02	$2.30\times10^{4} \pm 7.03\times10^{3}$
Poly[N,N’-bis(4-butylphenyl)-N,N’-bi-sphenylbenzidine] (Poly-TPD)	5.1~5.4[19–22]	0.01 ± 0.002	1.01 ± 0.36

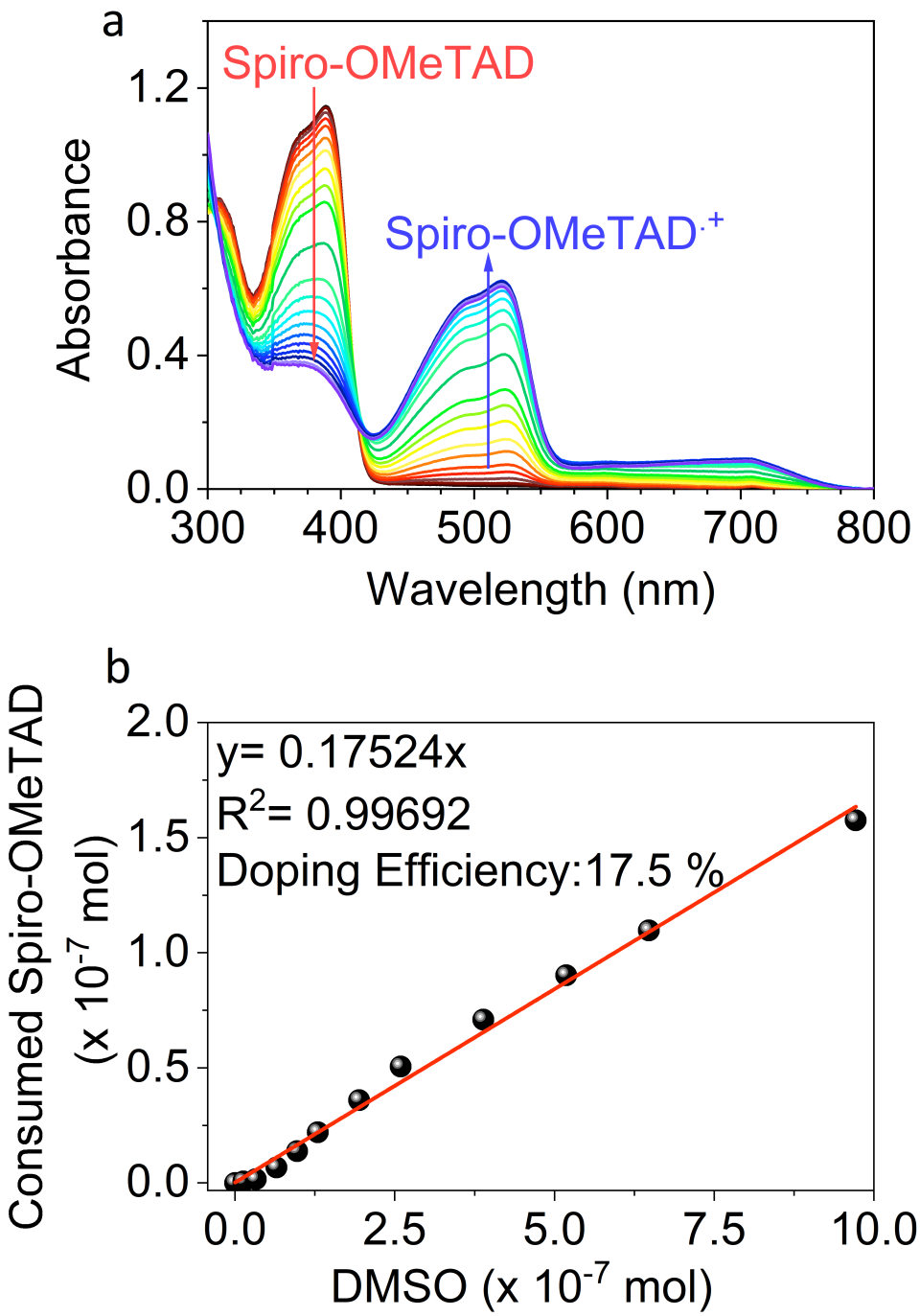

Supplementary Figure 1 | Evolution of UV-vis spectrum of Spiro-OMeTAD doping with DMSO-HBr via solution processing techniques. a, Evolution of absorption spectra of the Spiro-OMeTAD solution in chlorobenzene as a function of added DMSO-HBr adduct. **b**, Correlation plots for the consumption of Spiro-OMeTAD against the total amount of DMSO for the estimation of doping efficiency determined by UV-vis absorption. Red line shows the fitting result of plots by a linear fit ($y=ax$) where a indicates the doping efficiency.

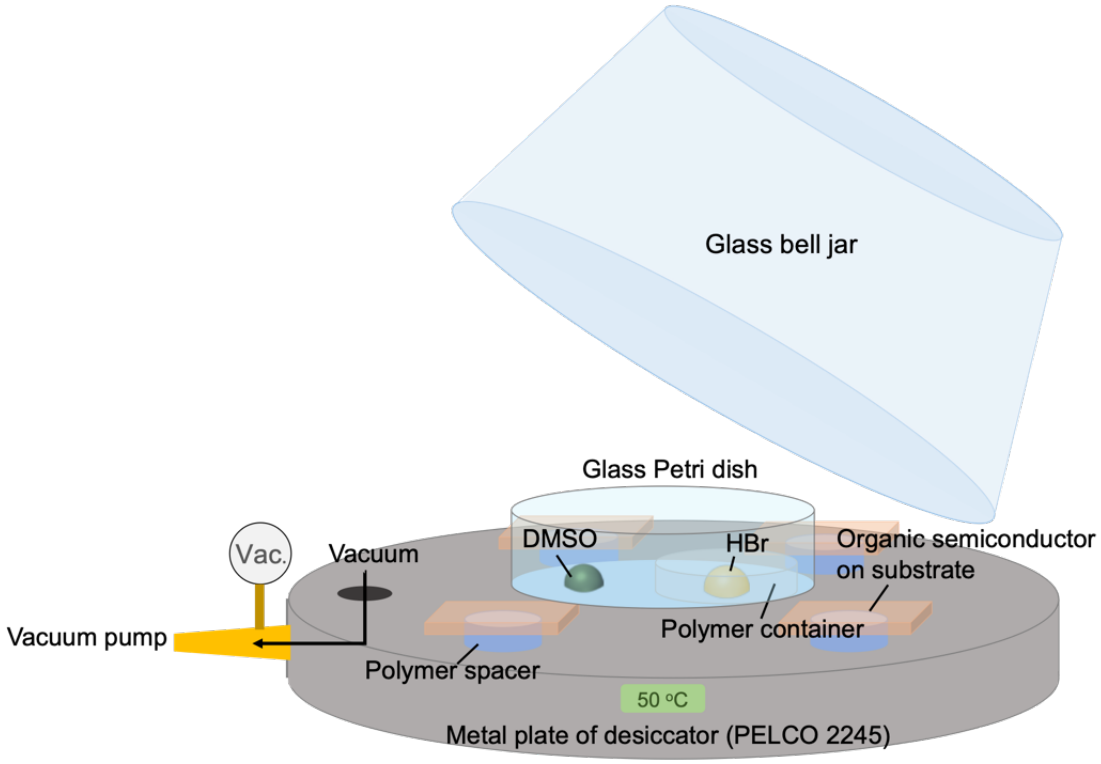

Supplementary Figure 2| Experimental set up for vapour process doping

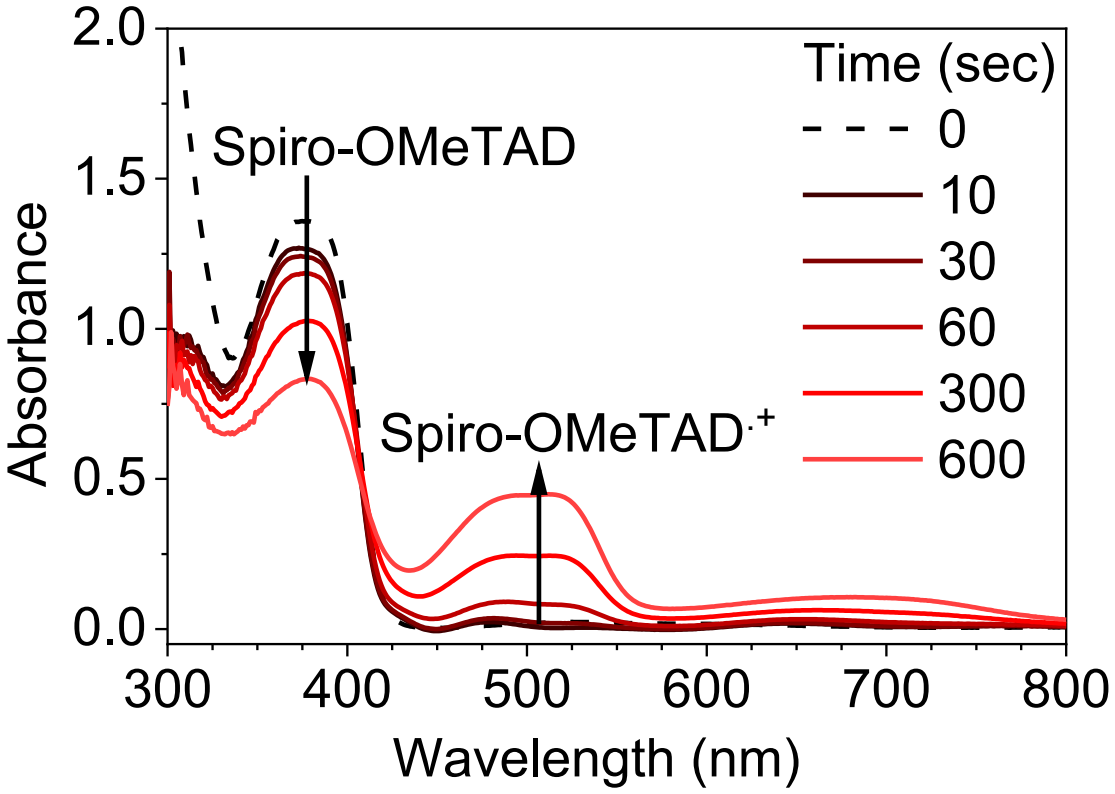

Supplementary Figure 3 | Evolution of UV-vis spectrum for Spiro-OMeTAD doped with DMSO-HBr via vapor phase processing. UV-vis absorption spectrum of a Spiro-OMeTAD thin film with the increasing exposure time in the DMSO and HBr vapour phase doping.

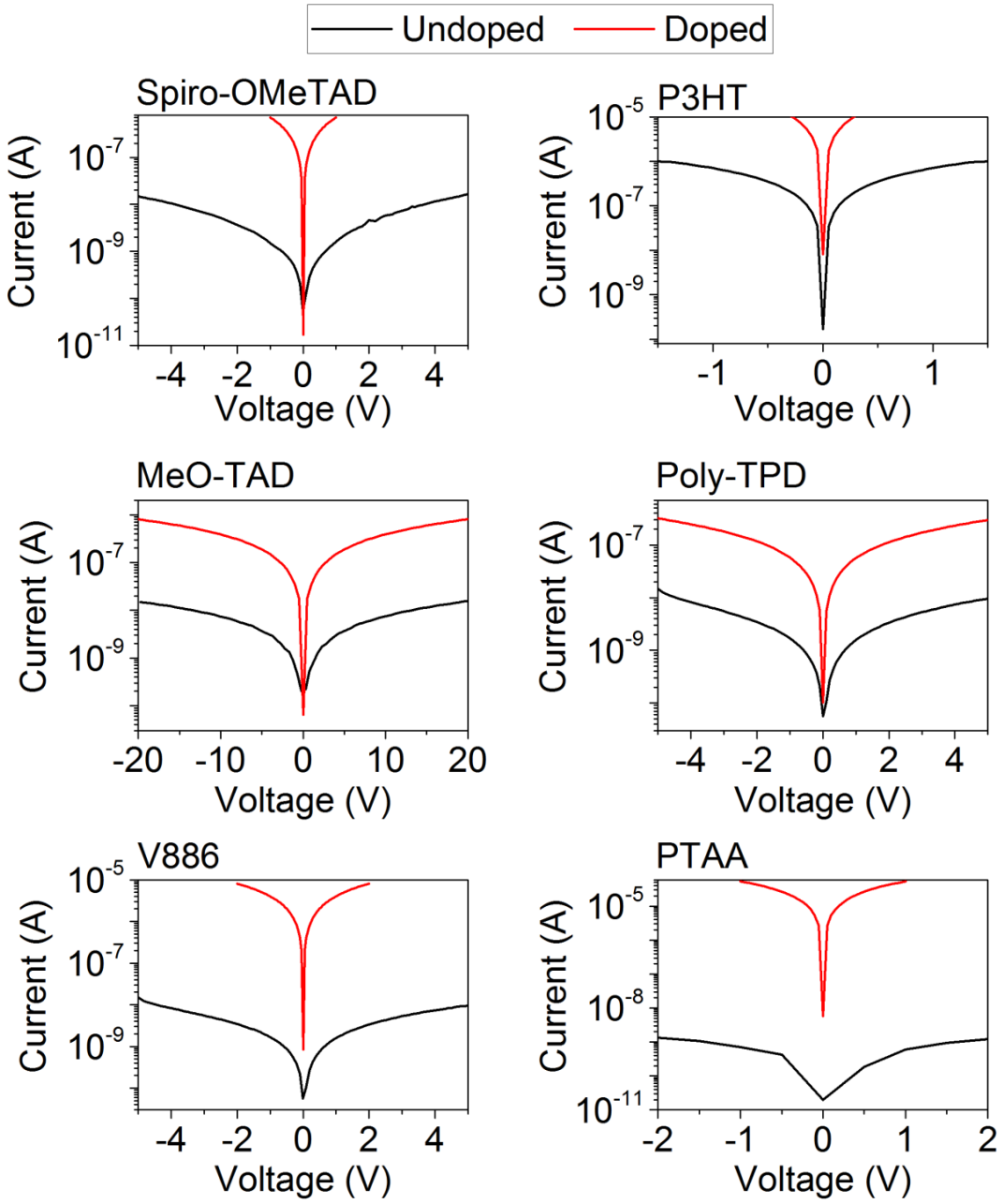

Supplementary Figure 4 | Doping of hole-transporting materials. Absolute current-voltage curves of thin film devices of HTMs before and after the doping with DMSO-HBr adduct in the vapour phase process. The film thickness of HTMs are 70-100 nm. Organic field-effect transistor (OFET) chips with bottom-gate and bottom-contact geometry with 30 nm gold/ITO interdigitated fingers of the source and drain contacts had varying channel lengths are used.

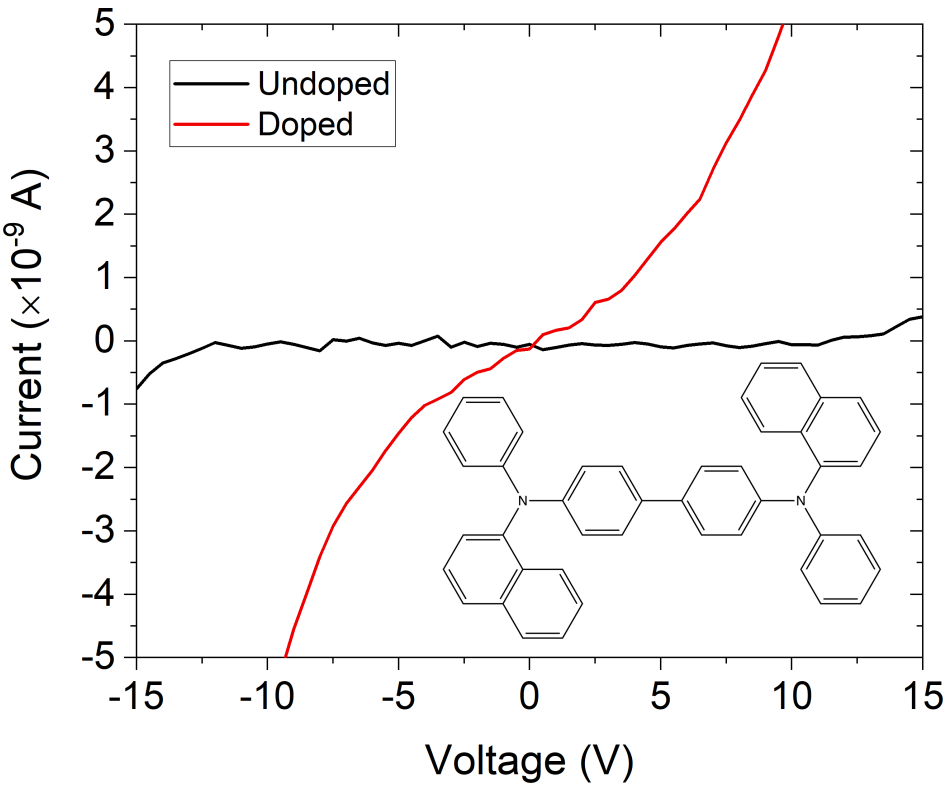

Supplementary Figure 5 | Doping of N,N′-Di(1-naphthyl)-N,N′-diphenyl-(1,1′-biphenyl)-4,4′-diamine (NPD). Current-voltage curves of thin film devices of NPD before and after the doping with DMSO-HBr adduct in the vapour phase process. IE of NPD is ~5.5eV[23]. The thickness of NPD film was ~100nm. Organic field-effect transistor (OFET) chips with bottom-gate and bottom-contact geometry with 30 nm gold/ITO interdigitated fingers of the source and drain contacts with 2.5µm channel lengths were used.

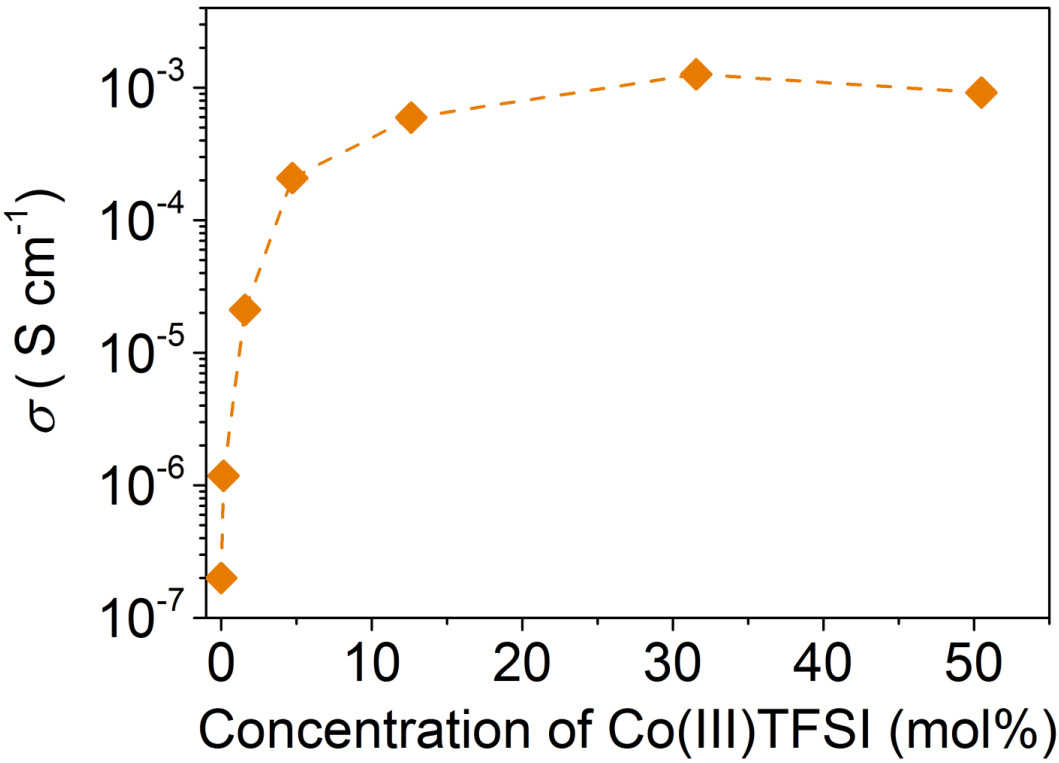

Supplementary Figure 6 | Conductivity of the Spiro-OMeTAD thin-film doped with tris(2-(1*H*-pyrazol-1-yl)-4-*tert*-butylpyridine)cobalt(III) tri[bis(trifluoromethane)sulfonimide] (FK209). Concentration: Concentration of FK209 with respect to Spiro-OMeTAD solution. The samples used an electrode pattern, designed for four-point probe measurements with a force channel length (direction of current flow) of 1 mm and a width of 1 cm and a sense channel length of 300 µm and width of 1 mm.

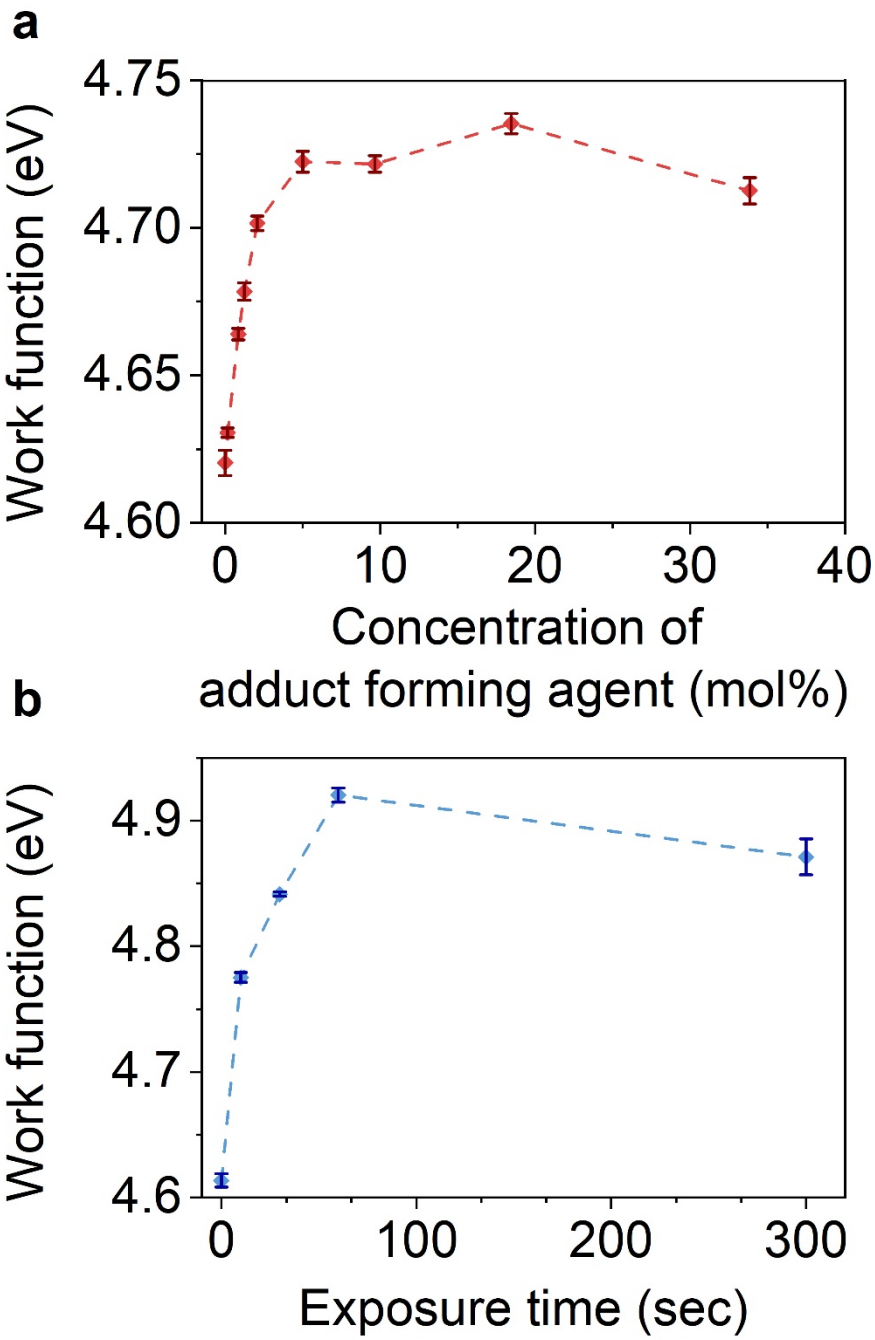

Supplementary Figure 7 | Change in work function of Spiro-OMeTAD thin films due to doping, measured by Kelvin probe. Spiro-OMeTAD thin film doped with DMSO-HBr adduct by **a**, the solution process and **b**, the vapour process. The concentration of adduct forming agent in the HTM solution was varied by changing the amount of adduct forming agent in the HTM solution. The thin films were deposited on F-doped SnO_2 glass (TEC 15, 15 Ω/sq). The thickness of HTM thin film is ~ 100 nm.

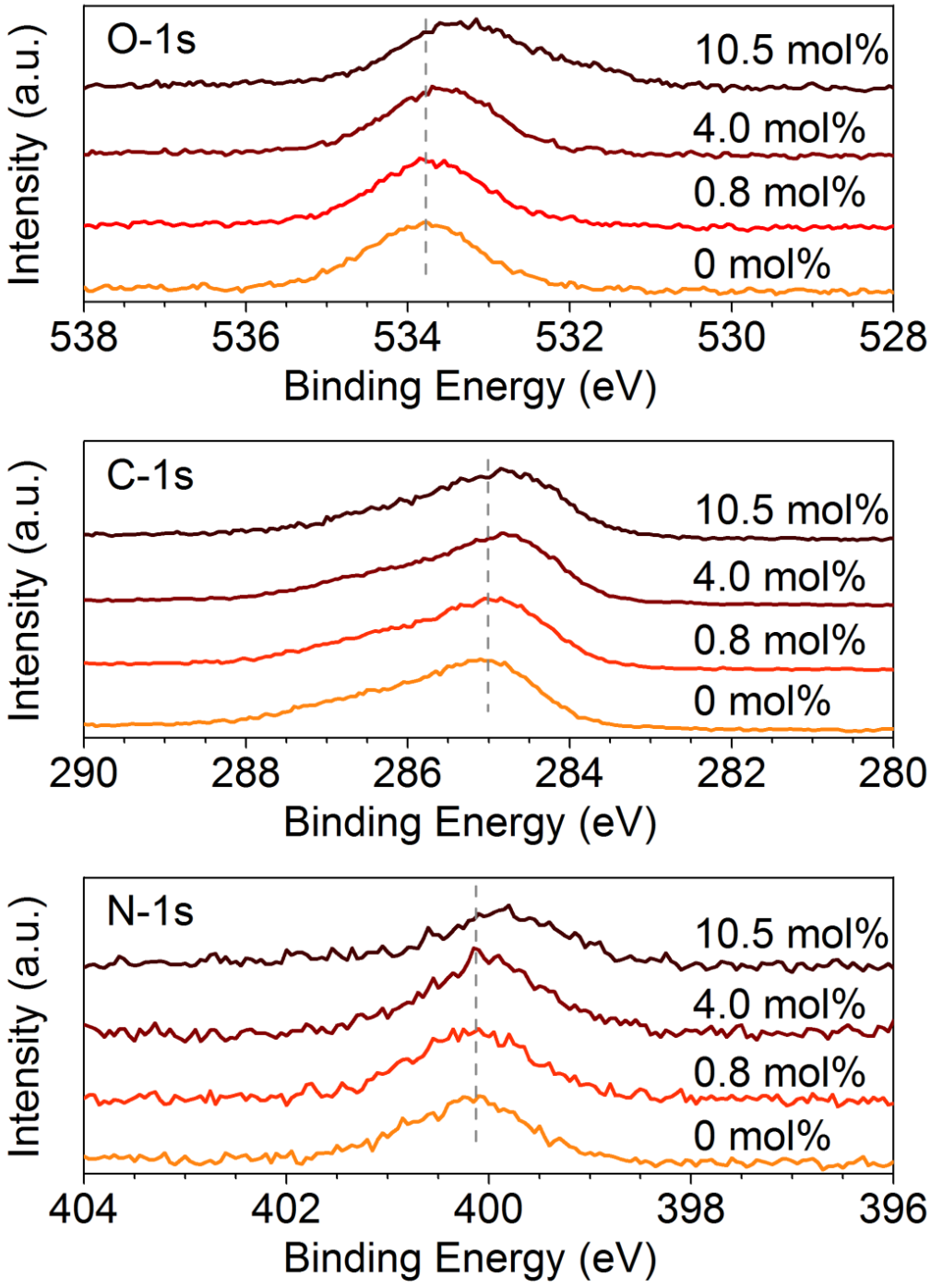

Supplementary Figure 8 | Evolution of XPS spectrum of the Spiro-OMeTAD thin film doped with DMSO-HBr by the solution process. X-ray photoelectron spectroscopy (XPS) spectra by O-1s, C-1s and N-1s core levels of the Spiro-OMeTAD thin film doped with different concentrations of adduct forming agent.

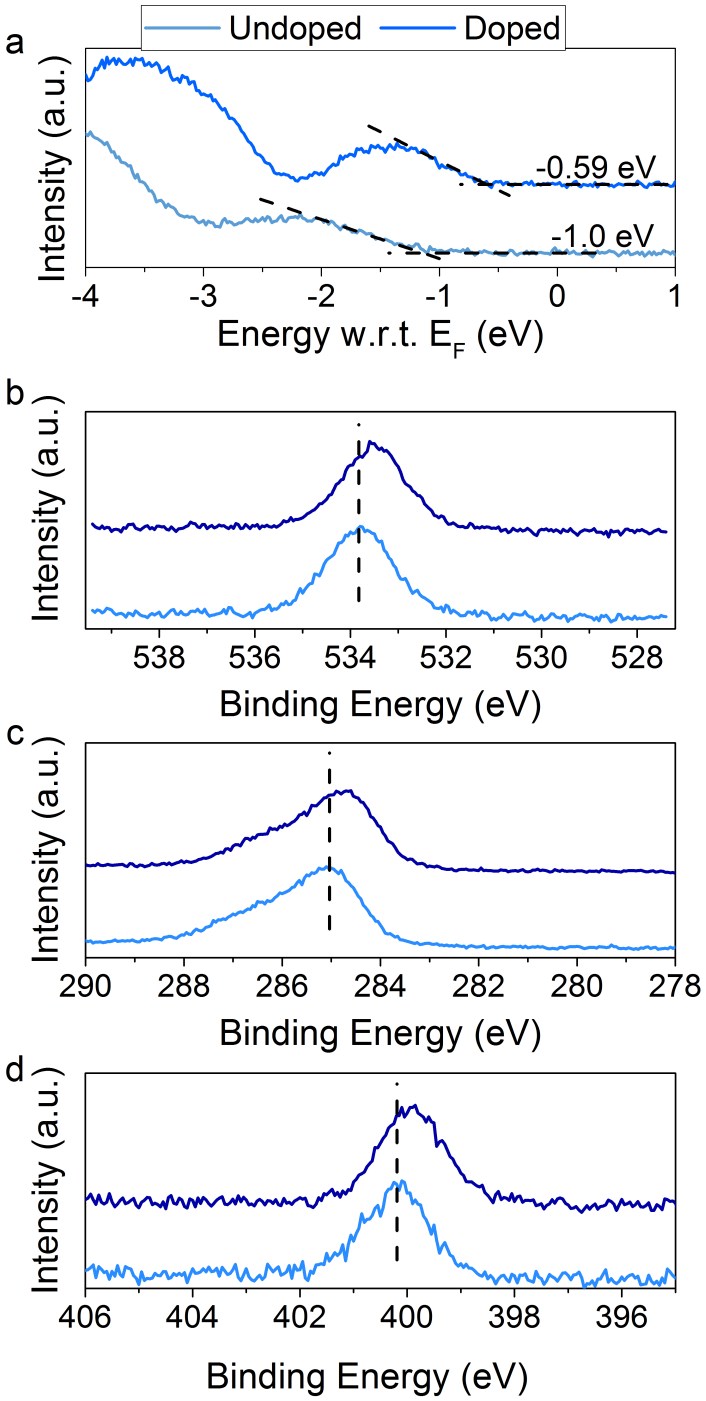

Supplementary Figure 9 | Evolution of UPS and XPS spectrum of the MeO-TPD thin film doped with DMSO-HBr by the solution process. a, UPS spectrum of the doped (with 5.25 mol% of adduct forming agent) and undoped MeO-TPD thin films. X-ray photoelectron spectroscopy (XPS) spectra of **b**, O-1s, **c**, C-1s and **d**, N-1s core levels of the doped and undoped MeO-TPD thin films.

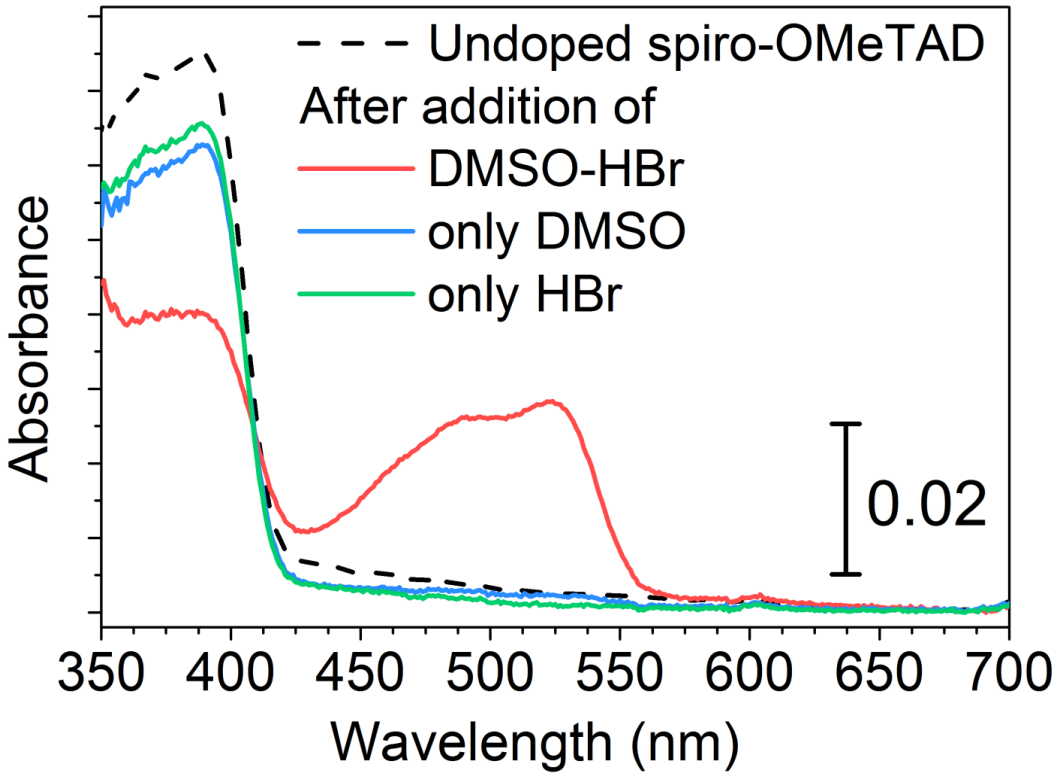

Supplementary Figure 10 | Doping ability of DMSO, HBr and the DMSO-HBr adduct in Spiro-OMeTAD solution. UV-vis absorption spectra of Spiro-OMeTAD solutions with only DMSO, HBr or the DMSO-HBr adduct.

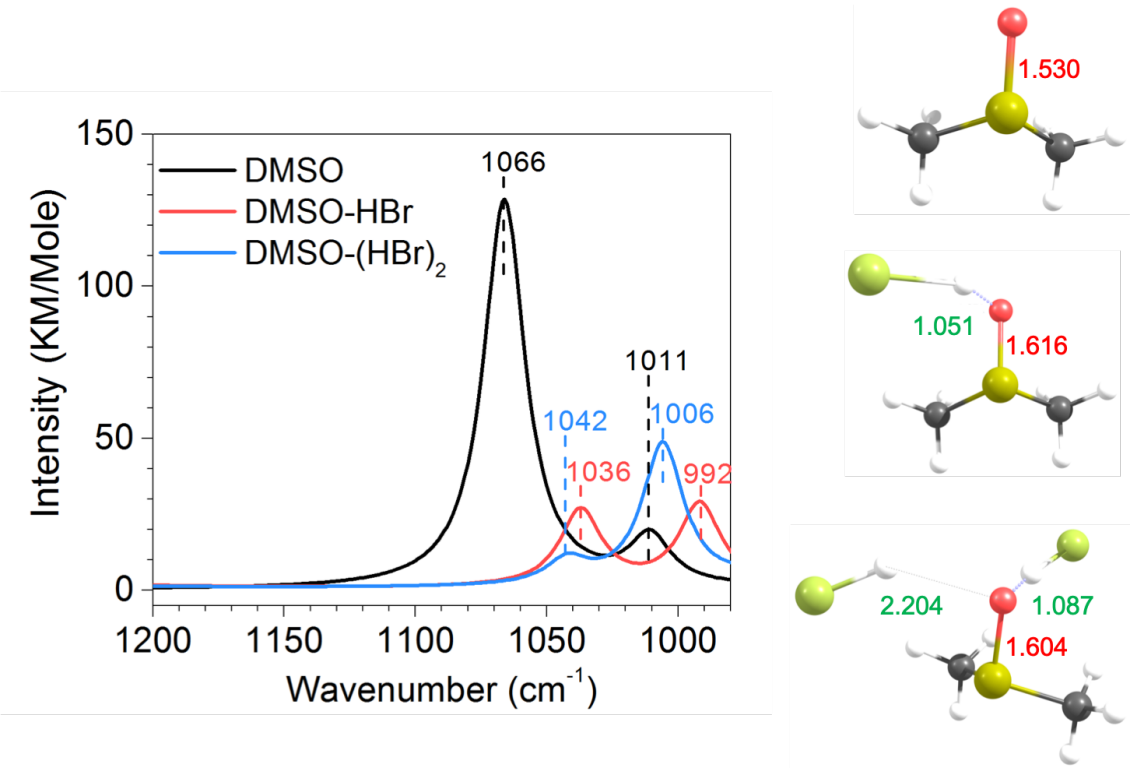

Supplementary Figure 11 | Quantum chemical calculations for the DMSO-HBr adduct. (Left) Calculated FTIR spectra of DMSO, DMSO-HBr, and DMSO-$(HBr)_2$. (Right) Simulated chemical structure of DMSO, DMSO-HBr, and DMSO-$(HBr)_2$ adduct. (S, O, C, Br and H atoms are represented by the yellow, red, black, green and grey-white spheres. Numbers show bond lengths of S-O bond and O-H bond. Numbers present bond length (Å) of S=O (Red) and O-H (Green).

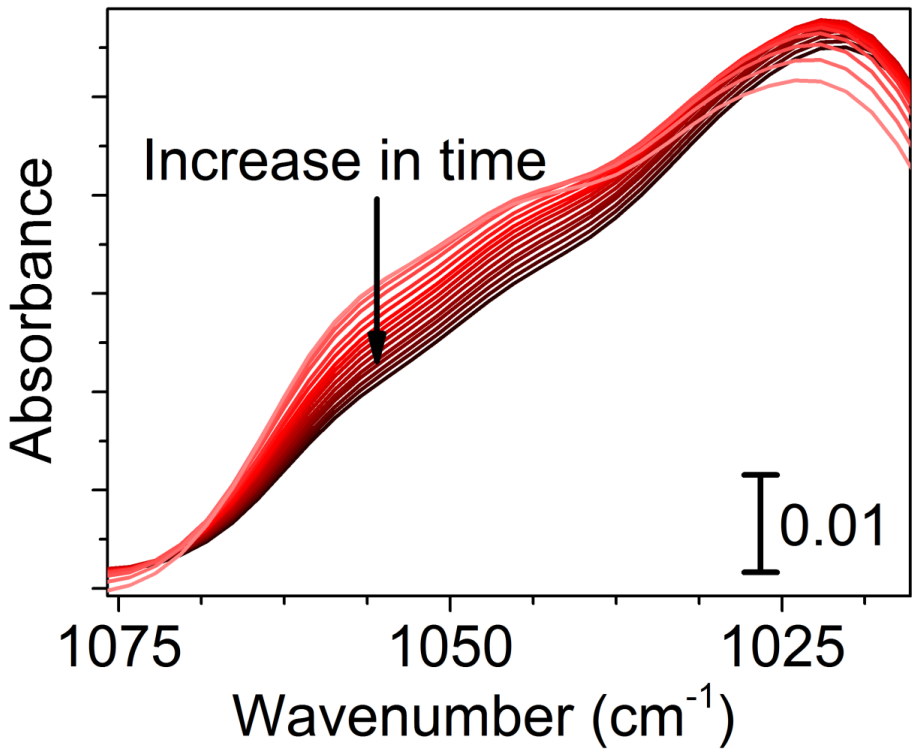

Supplementary Figure 12 | Evolution of FTIR spectrum during DMSO-HBr doping in the solution. The consumption of the adduct during the doping process as seen in a series of FTIR spectra recorded at different time intervals.

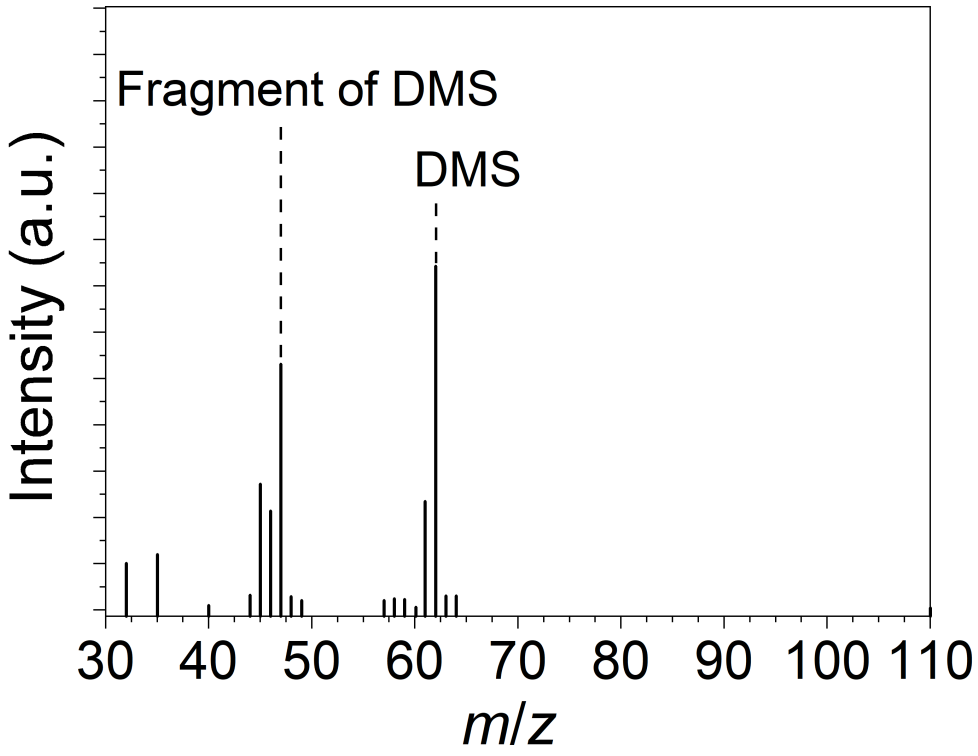

Supplementary Figure 13 | Determination of by-product during DMSO-HBr doping by solution process. GC-MS spectra of the by-product(s) during the doping process.

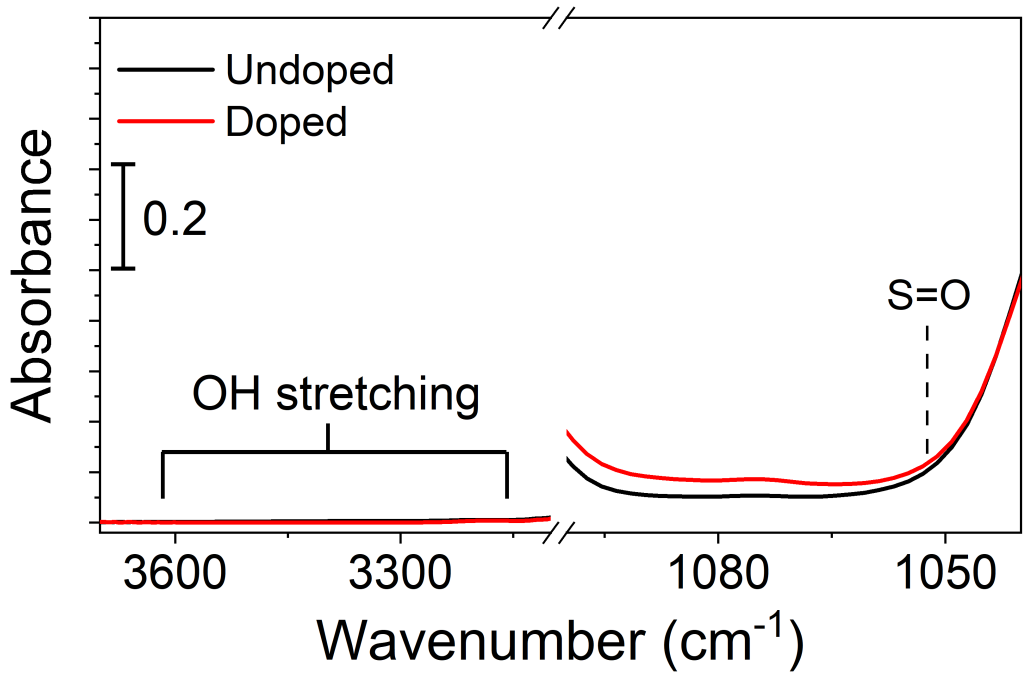

Supplementary Figure 14 | Determination of remaining molecule on the Spiro-OMeTAD thin film after DMSO-HBr doping by solution process. FTIR spectra of doped Spiro-OMeTAD thin film with DMSO-HBr by solution process. The region of S=O absorbance and the region of the H_2O absorbance.

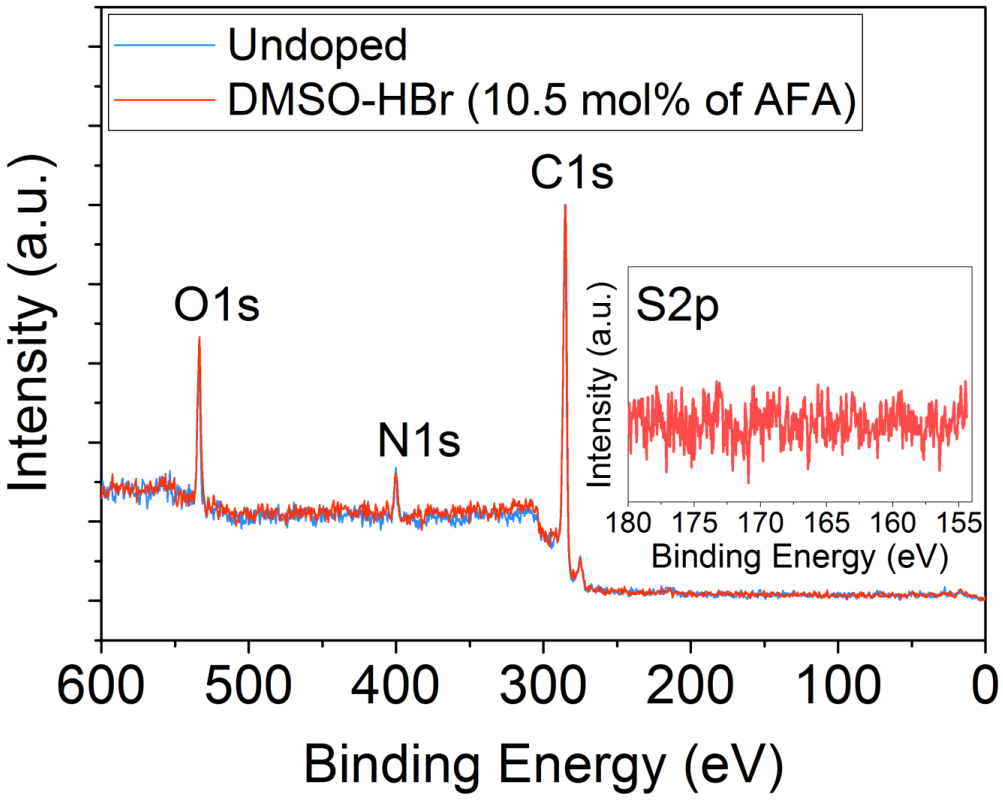

Supplementary Figure 15 | Difference of XPS spectra of the Spiro-OMeTAD thin film doped with DMSO-HBr by solution process. XPS spectrum of the undoped Spiro-OMeTAD thin film and the thin film doped with 10.5 mol% of adduct forming agent. Inset: XPS spectrum at S-2p on the film doped with 10 mol% of adduct forming agent.

Supplementary Note 1: *Clean doping*

We do not observe absorbance for Sulfur in XPS spectra of doped films, which indicates that the doping process is "clean", in that it does not leave behind by-products or unreacted dopants in the organic semiconductor matrix - containing only doped HTM and counter ions after the doping reaction.

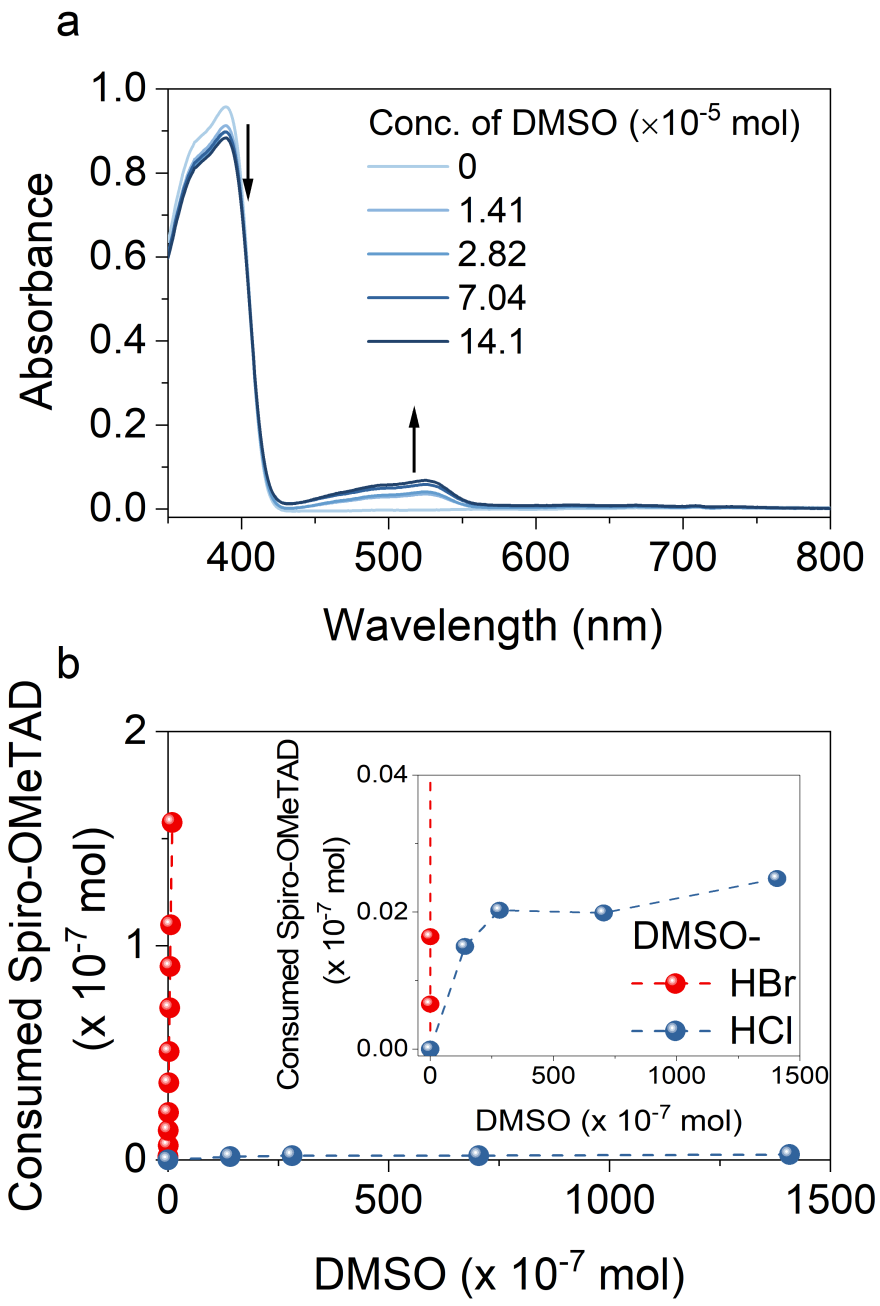

Supplementary Figure 16 | Evolution of UV-vis spectrum of Spiro-OMeTAD solution with the addition of DMSO-HCl. a, Evolution of absorption spectra of the Spiro-OMeTAD solution in chlorobenzene as a function of added DMSO-HCl adduct. **b**, Correlation plots for the consumption of Spiro-OMeTAD, determined by UV-vis absorption, against the total amount of adducts, represented by DMSO concentration. The data for DMSO-HBr and DMSO-HCl adducts are plotted together to compare their doping efficiency.

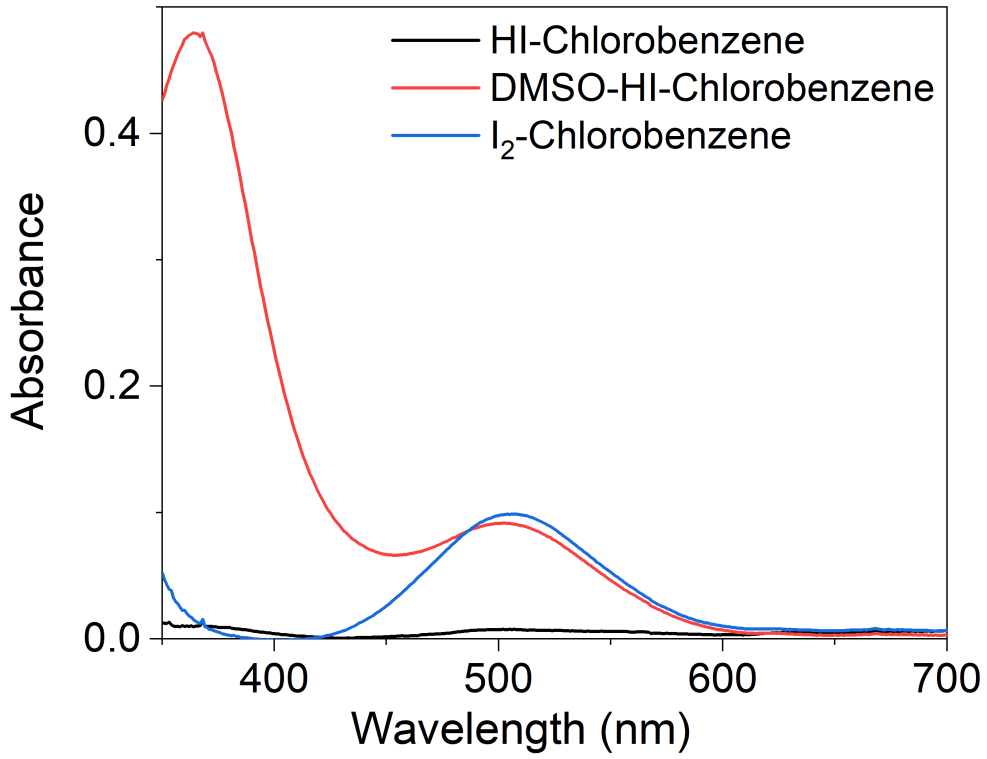

Supplementary Figure 17 | UV-vis spectrum of DMSO-HI adduct. a. Absorption spectra of HI w/ and w/o DMSO in chlorobenzene. The absorption spectrum of I_2 in chlorobenzene is provided for the comparison.

Supplementary Table 2 | S-O bond length of DMSO-HX adducts.

HX type	S-O bond length (Å) in DMSO-HX	S-O bond length (Å) in DMSO-$(HX)_2$
No HX	1.530	1.530
HCl	1.599	1.581
HBr	1.616	1.603
HI	1.623	1.607

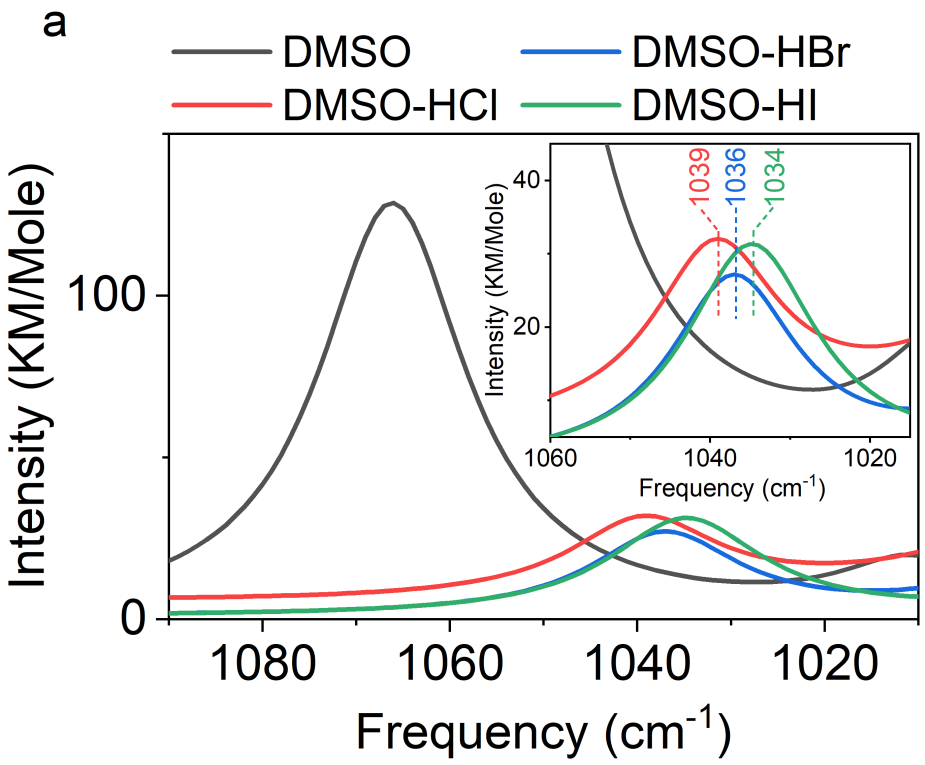

Supplementary Figure 18 | Quantum chemical calculations for the DMSO-HX adduct. a. Calculated FTIR spectra of DMSO, DMSO-HCl, DMSO-HBr and DMSO-HI. Inset: FTIR spectra magnified between 1010 cm^{-1} to 1060 cm^{-1}.

Supplementary Note 2: *Relative strength of DMSO-HX (X= Cl, Br or I) in p-type doping*

In a similar fashion to DMSO-HBr, the DMSO-HCl adduct also induces p-type doping. However, we observe that the doping ability of the DMSO-HCl adduct is much weaker (Supplementary Fig. 16). At the opposite end of the scale, the DMSO-HI adduct is unstable in ambient conditions and a considerable amount of I_2 is produced due to the oxidation of I^- in the solution, which we detect by UV-Vis spectroscopy (Supplementary Fig. 17). We find that the DMSO-HX interaction strength progressively reduces with HI > HBr > HCl. This is a consequence of the reduction in the S-O bond length (Supplementary Table 2) and increase in the S-O vibration frequency (Supplementary Fig. 18) when going from I to Cl, which we have ratified computationally.

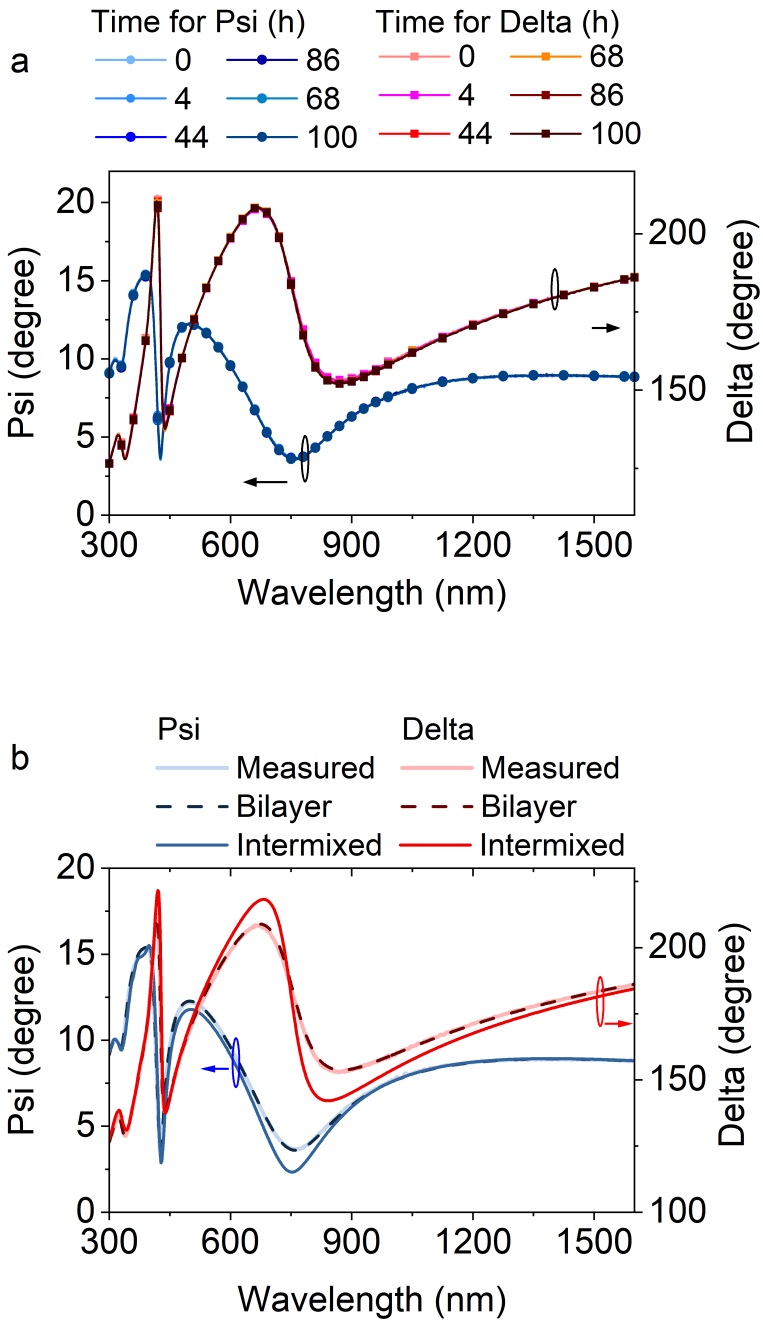

Supplementary Figure 19 | Ellipsometry profile after thermal stress. a. Ellipsometry profile Ψ and Δ of an un-doped MeO-TPD thin film on top of a heavily doped MeO-TPD thin film measured after thermal stress (at 55 °C up to 100 h). **b**. Observed and simulated ellipsometric profiles for the stacked layers of undoped and doped thin film.

Supplementary Note 3: *Analysis of ellipsometric profiles of stacked organic layers*
We fit the ellipsometric profile of the thin-film used for thermal stability study as a bilayer stack with the bottom layer as doped MeO-TPD (~150 nm) and the top layer (~100 nm) as un-doped MeO-TPD. We fit both the layers for thicknesses first using Cauchy model and then for refractive indices using B-spline function. The Δ and Ψ spectra fit well to the expected double-layer stack of doped and intrinsic MeO-TPD layers, both before and after the thermal stressing. For completeness, using an effective medium approximation[24], we simulate the ellipsometric profile which would be expected if the doped and non-doped layers mix to form a single homogeneous film. The simulated profiles for the mixed films, are different than the observed profiles (Supplementary Fig. 19b), confirming that the migration of the doped material (or counterion) does not happen during the 50˚C 100 hour stress test.

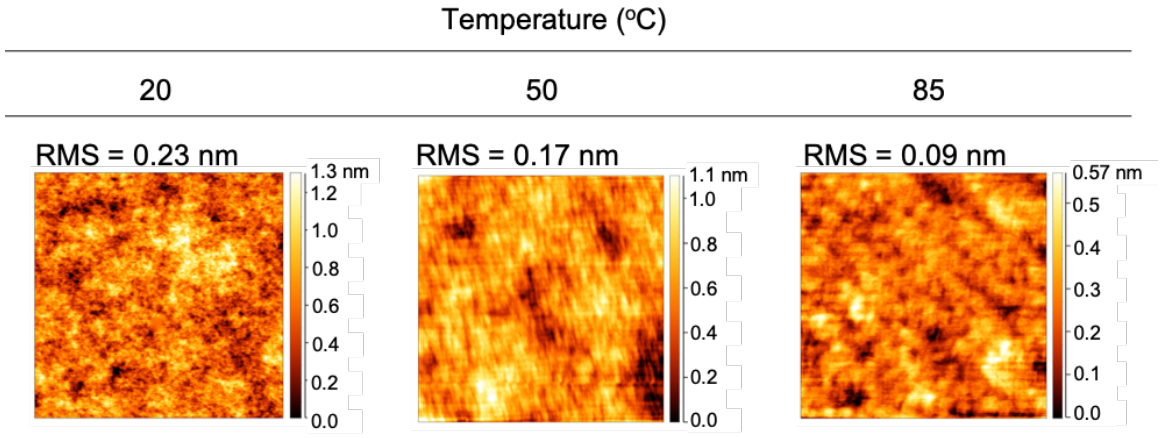

Supplementary Figure 20 | Atomic force microscope (AFM) images of the doped MeO-TPD film with DMSO-HBr. The doped film (with 10 mol% of adduct forming agent) is annealed at different temperatures for 10 minutes. AFM scanning area is 2×2 μm. The Root Mean Square (RMS) value is evaluated over all pixels in a single AFM image.

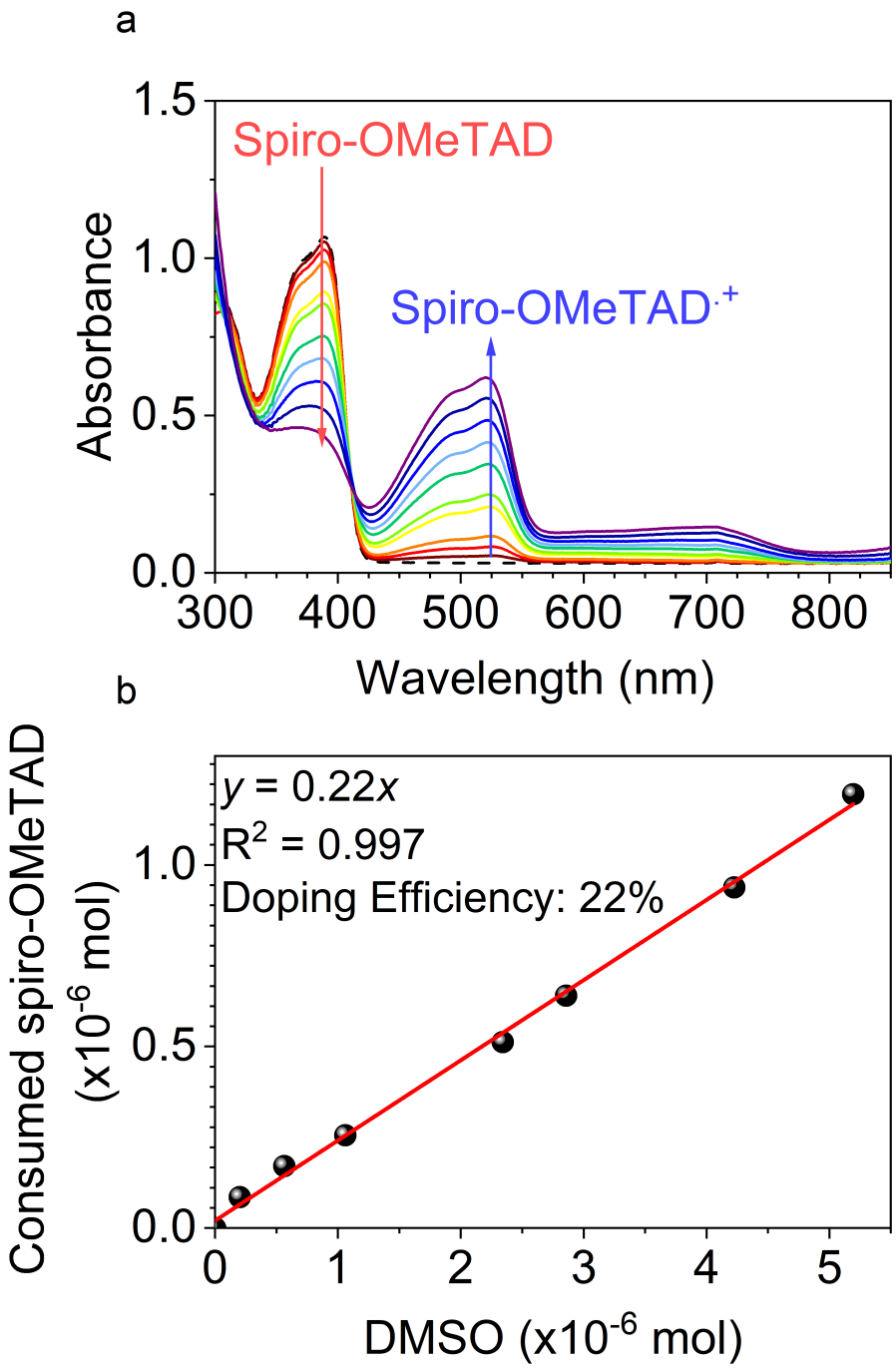

Supplementary Figure 21 | Evolution of UV-vis spectrum of Spiro-OMeTAD doped with DMSO-HBr-CSA by the solution process. a, Absorption spectra of Spiro-OMeTAD solution in chlorobenzene with an increase in concentration of DMSO-HBr-CSA (~1:0.09:1 molar ratio). **b**, Correlation plots for the consumption of Spiro-OMeTAD against the total amount of DMSO present in the dopant for the estimation of doping efficiency. The concentration of consumed Spiro-OMeTAD is determined by UV-vis absorption and the known exciton coefficient of Spiro-OMeTAD solution. Red line shows the fitted line for a linear fit (i.e. $y=ax$) where a indicates the doping efficiency.

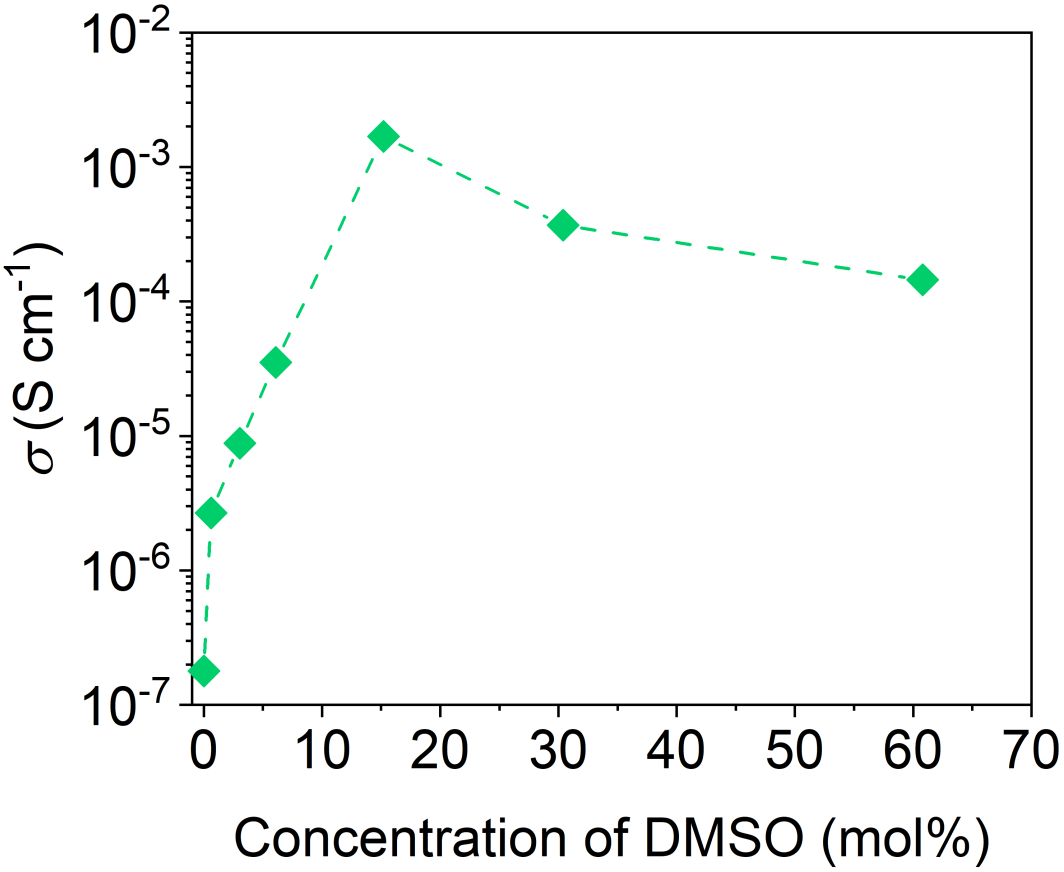

Supplementary Figure 22 | Conductivity of the Spiro-OMeTAD thin-film doped with DMSO-HBr-CSA. Molar Concentration of DMSO in DMSO-HBr-CSA adduct (~1:0.09:1 molar ratio). The samples is used an electrode pattern, which is designed for four-point probe measurements with a force channel length (direction of current flow) of 1 mm and a width of 1 cm and a sense channel length of 300 μm and width of 1 mm.

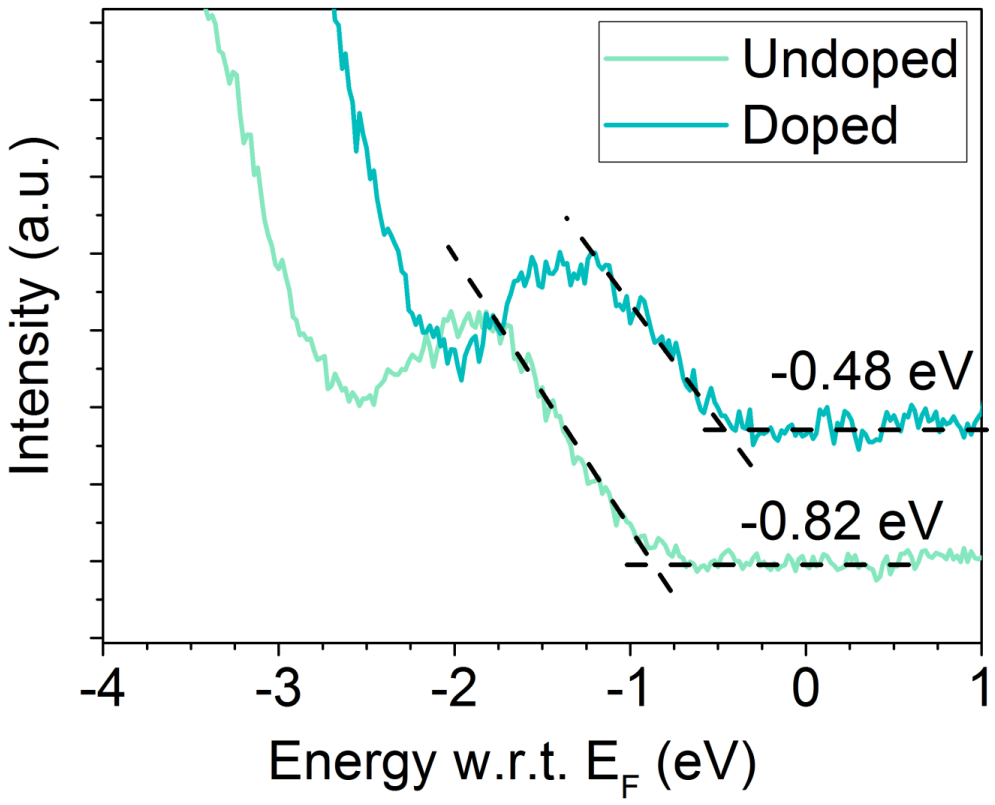

Supplementary Figure 23 | UPS spectra of undoped and doped Spiro-OMeTAD thin-films. The doping is via DMSO-HBr-CSA. The Spiro-OMeTAD film doped with 13 mol% of adduct forming agent for DMSO-HBr-CSA doping.

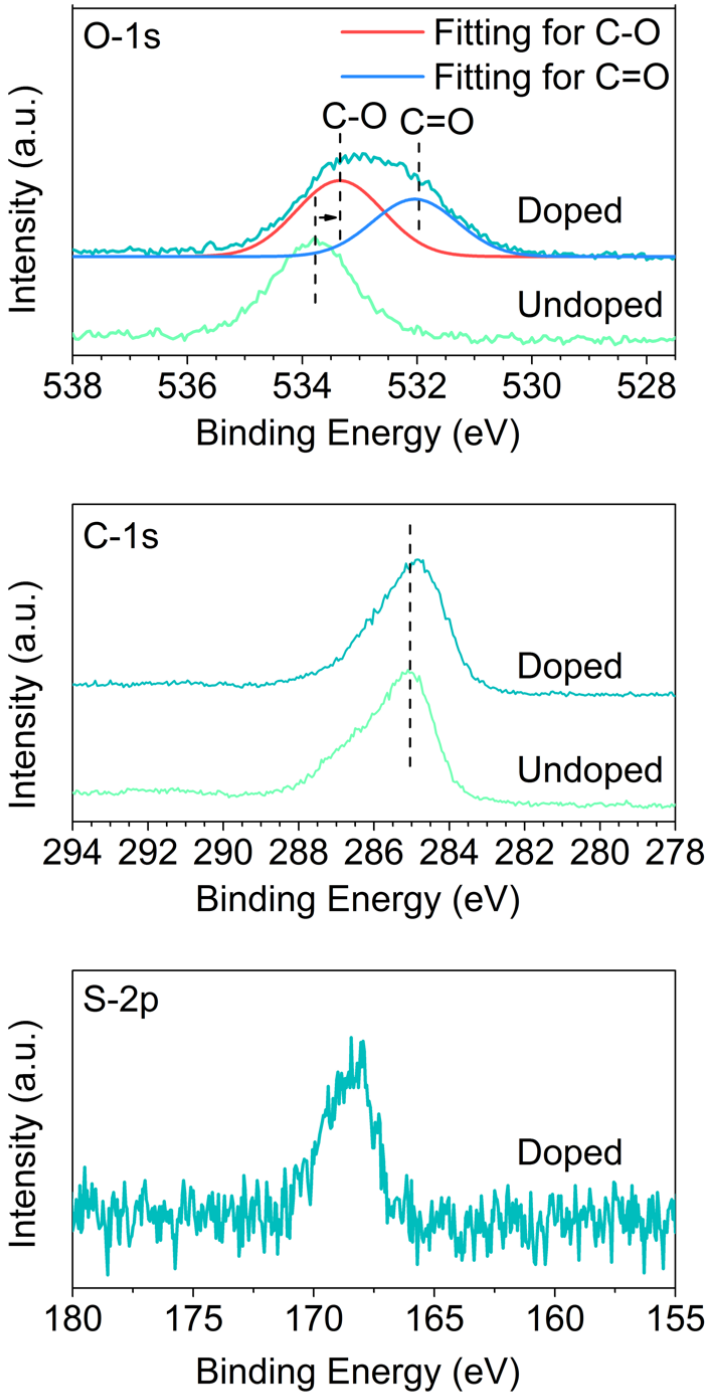

Supplementary Figure 24 | Evolution of XPS spectrum of the Spiro-OMeTAD thin film doped with DMSO-HBr-CSA. X-ray photoelectron spectroscopy (XPS) spectra of the O-1s, C-1s and S-2p core levels of the Spiro-OMeTAD thin film doped with 13 mol% of adduct forming agent for DMSO-HBr-CSA doping.

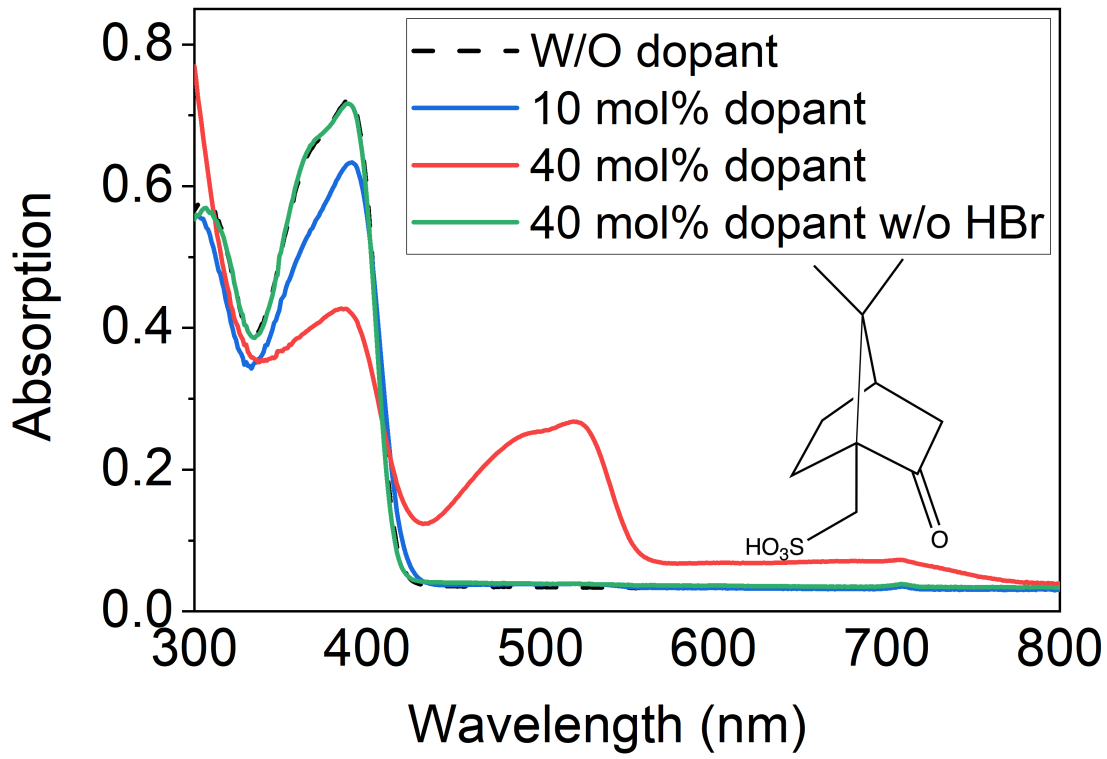

Supplementary Figure 25 | 10-camphorsulfonic acid (CSA) as a source for the counter ion UV-vis absorption spectra of Spiro-OMeTAD solution doped with DMSO-HBr-CSA and DMSO-CSA (i.e. dopant w/o HBr). Inset: Chemical structure of CSA.

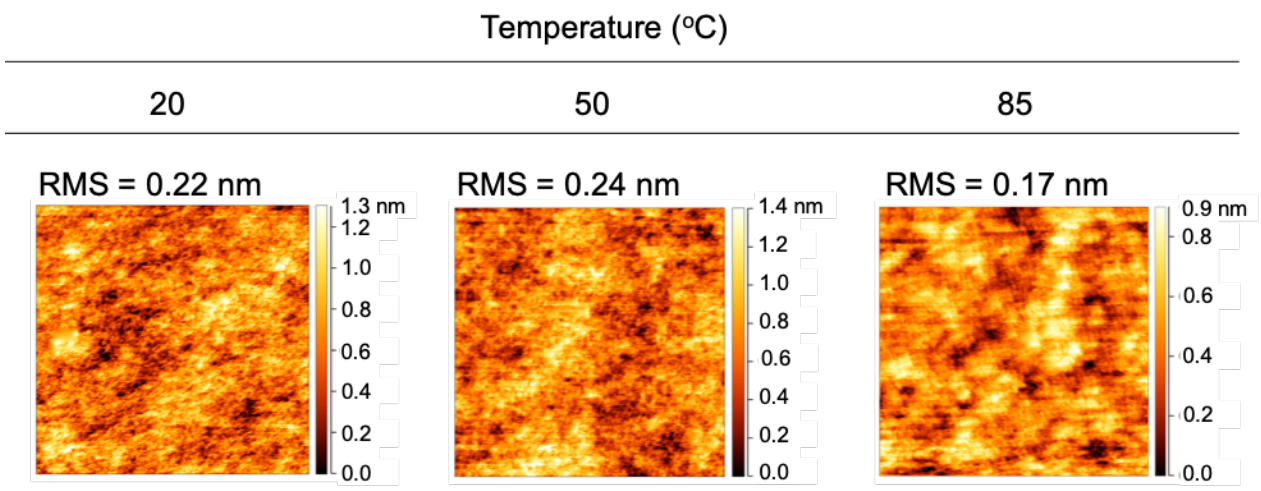

Supplementary Figure 26 | Atomic force microscope (AFM) images of the doped MeO-TPD film with DMSO-HBr-CSA. The doped film (with 10 mol% of adduct forming agent) is annealed at different temperatures for 10 minutes. AFM scanning area is 2×2 μm^2. The Root Mean Square (RMS) value is evaluated over all pixels in a single AFM image.

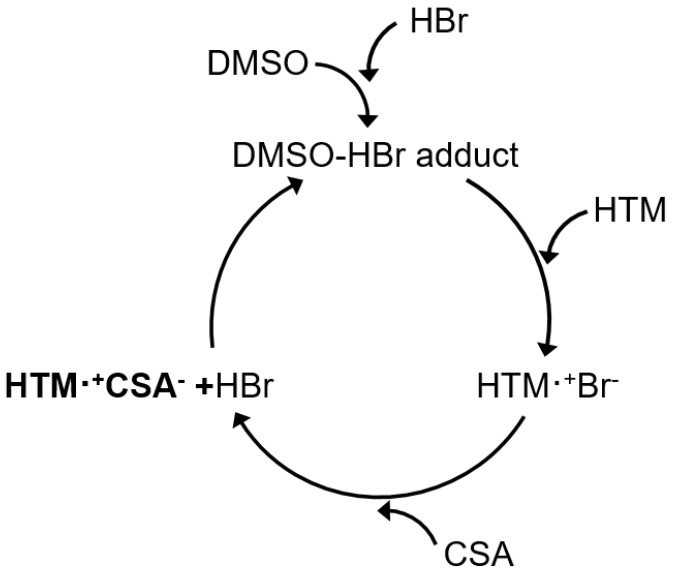

Supplementary Figure 27 | Decoupling and doping process. The proposed process of decoupling and doping with the chosen counter ion assisted by DMSO-HBr adduct. Acronyms are denoted as 10-camphorsulfonic acid (CSA), dimethyl sulfoxide (DMSO), hydrobromic acid (HBr), and hole-transporting material (HTM).

Supplementary Note 4: *Mechanism of Doping process by the DMSO-HBr-CSA*

We rationalize the doping process by the DMSO-HBr-CSA system considering that while DMSO and HBr form the adduct responsible for doping, CSA can provide the counter ion in the form of 10-camphorsulfonate and the HBr can be subsequently regenerated for further doping (Supplementary Fig. 27).

Supplementary Note 5: *Molecular organic semiconductor salts*

Our new doping process can also be used to produce very "clean" molecular organic semiconductor salts, such as Spiro-OMeTAD^{+} TFSI^{-}, which have been used as efficient and stable dopants in recent reports[25,26]

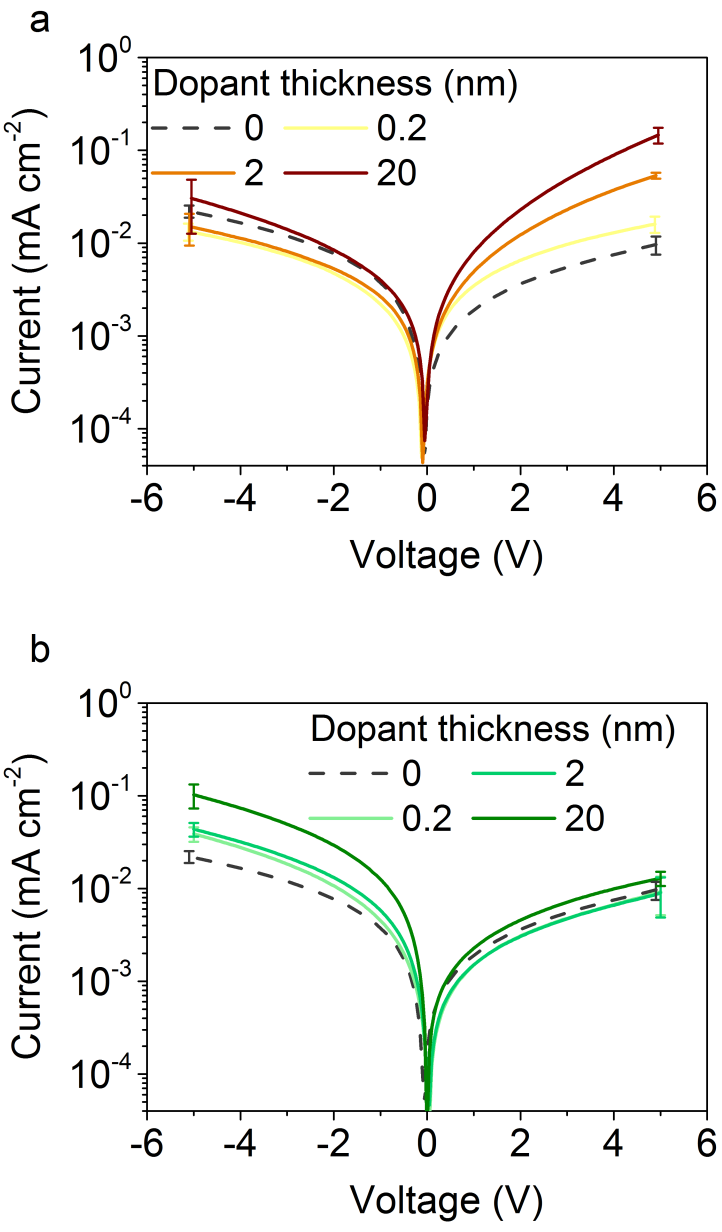

Supplementary Figure 28 | Current density-voltage curves of the hole-only devices with interfacial doping at one interface. a, doping at the Poly-TPD:Au interface **b**, at the FTO:Poly-TPD interface. The thickness of Poly-TPD in the devices is ~700 nm. The graded doping is controlled by adding different concentration.

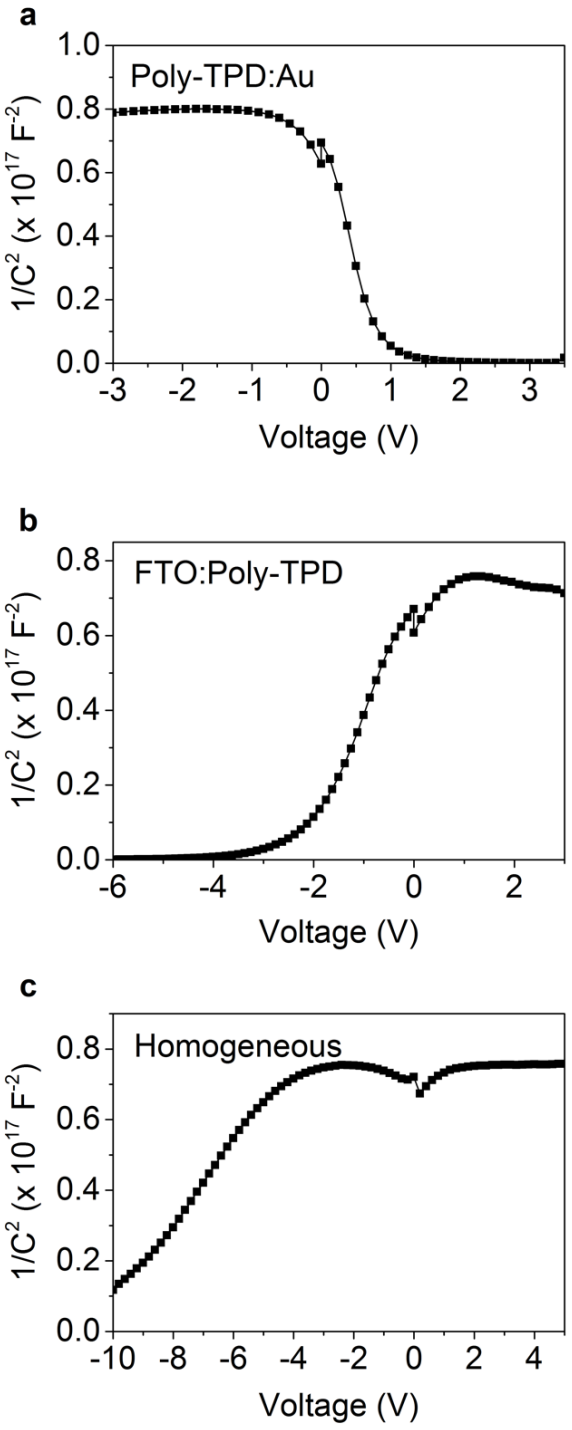

Supplementary Figure 29 | $1/C^2$-voltage curves of the hole-only devices doped at different interfaces. a, doping at Poly-TPD: Au interface, **b**, at FTO: Poly-TPD interface and **c**, homogeneous doping. Thickness of Poly-TPD in the devices is ~350 nm.

Supplementary Note 6: *Acceptor density when the depletion width approaches the total film thickness*
Since the calculated N_A increased strongly for all devices (doped or undoped) when the depletion width approaches the total film thickness, (whether this is approaching the Au or FTO electrode) we assume that this is an artefact of the measurement, rather than carrying real physical meaning. Our capacitance-voltage results are consistent with asymmetric doping but are subject to a model and the assumption of which contact is the primary contact being probed.

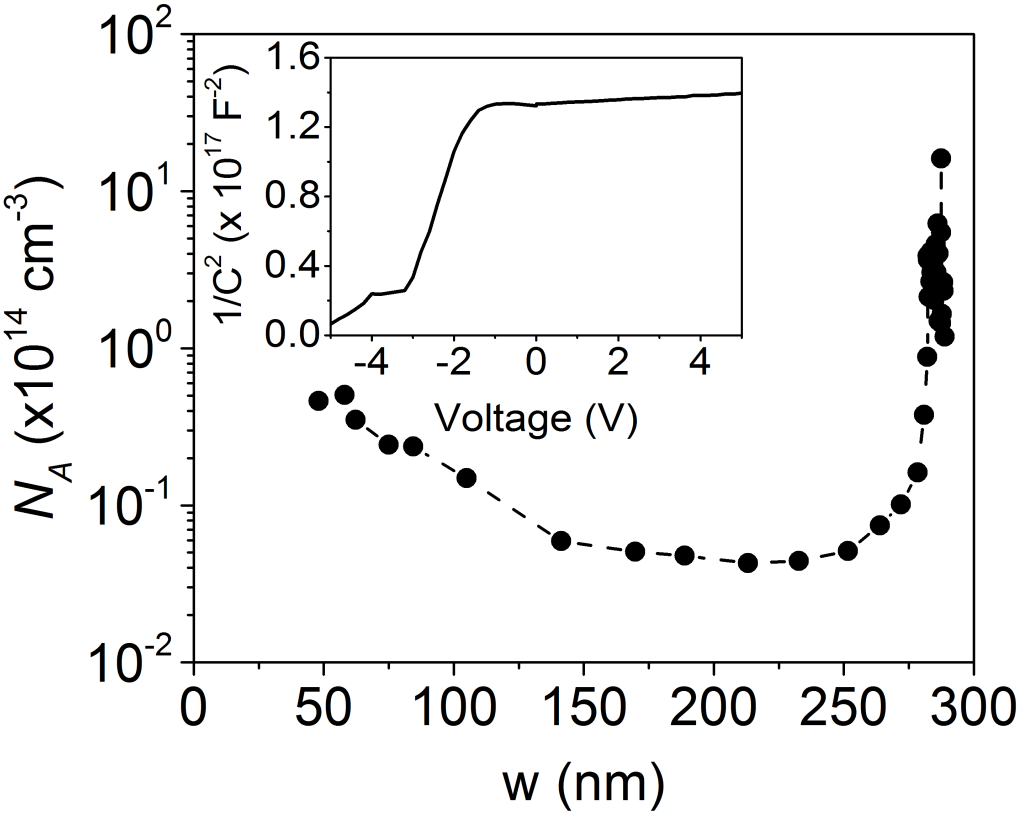

Supplementary Figure 30 | Acceptor density (N_A) profile of undoped hole-only devices. Acceptor density (NA) as a depletion width (w) of the hole-only devices with undoped Poly-TPD (~350 nm), inset: $1/C^2$-voltage curves of the hole-only devices.

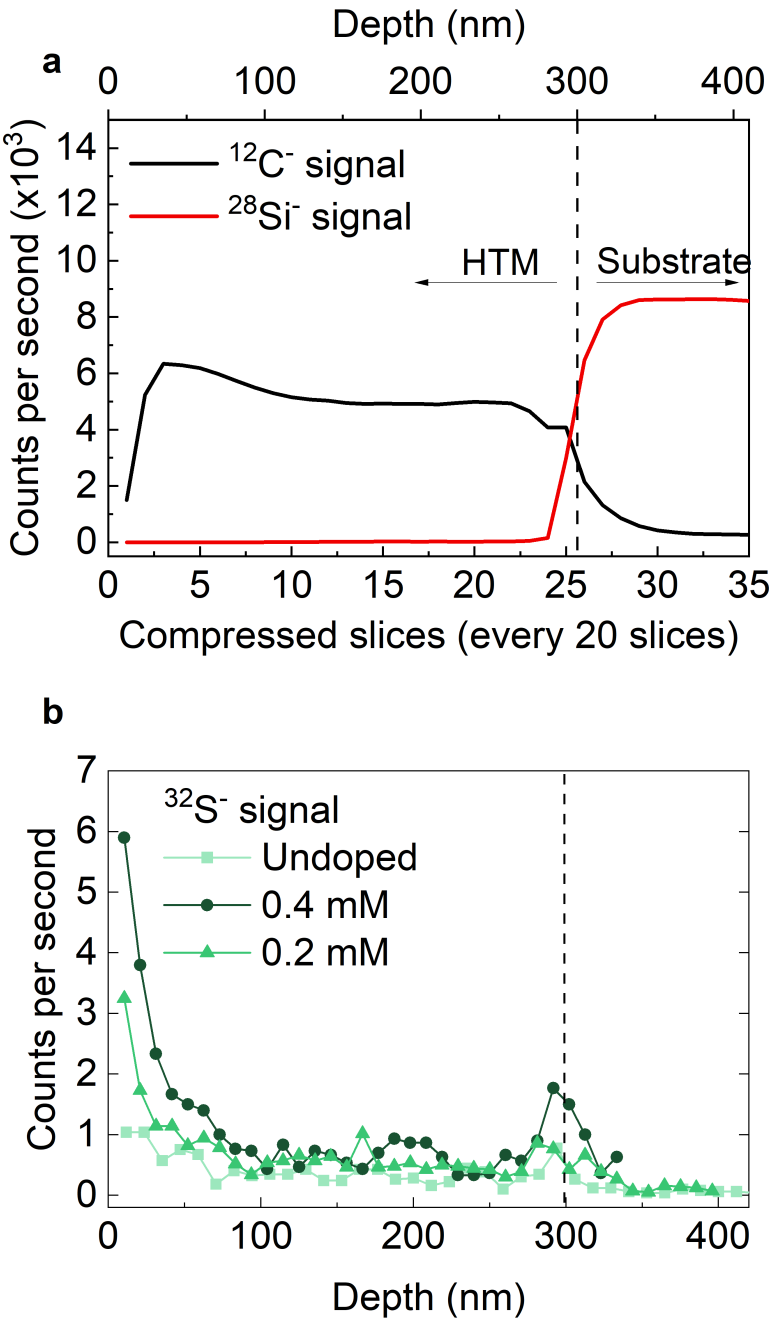

Supplementary Figure 31 | Secondary Ion Mass Spectrometry profile of poly-TPD films on Si substrates. a. $^{12}C^-$ and $^{28}Si^-$ signals for the calibration of Poly-TPD/Si interface location using the half intensity of $^{28}Si^-$ signal. The poly-TPD layer thickness is ~300 nm measured by surface profiler. **b**. $^{32}S^-$ signal of the undoped film and the asymmetrically doped film at the Poly-TPD:Air interface with different adduct-forming agent (DMSO-HBr-CSA) concentration.

Supplementary Note 7: *$^{32}S^-$ signal at the opposite interfaces*

We do note that there is a relatively small increase in the $^{32}S^-$ signal at the opposite interfaces to where the doping was intended, which indicates some degree of diffusion of the counter-ions during fabrication.

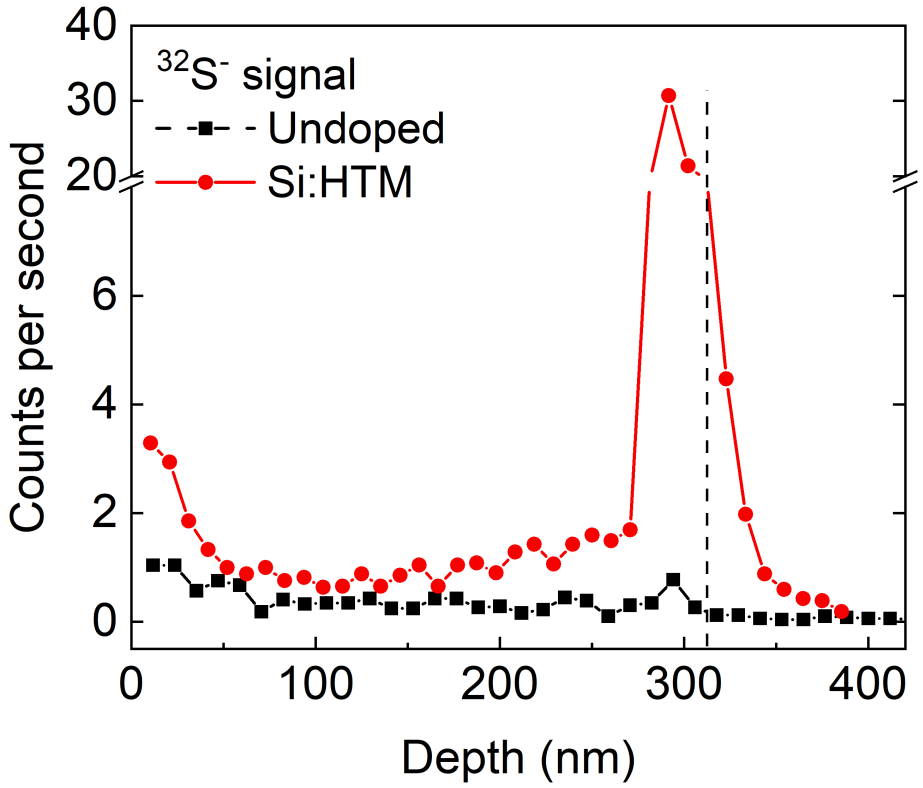

Supplementary Figure 32 | $^{32}S^-$ signal profile of the Poly-TPD films on Si substrate doped at the Si:HTM interface, measured by Secondary Ion Mass Spectrometry.

Supplementary Note 8: *Organic thin film transistor (OTFT)*

From the obtained ΔN_{tr}, we note that both the DMSO-HBr (M) and DMSO-HBr (H) devices benefit from the p-doping effect with an effective reduction in the surface trap density on the order of 10^{11} cm^{-2}. On the other hand, from the derived trap concentration for unit energy, D_{tr}, we found that the DMSO-HBr (M) device exhibits the least subthreshold trap states, which indicate a potential trap-filling effect could be enabled by our adduct approach. We obverse improvement in field-effect mobility (Supplementary Table 3) that is comparable to what has been reported in the literature[27] but the need of employing any contact modifier for hole injection. Therefore, we can confirm that adding a moderate amount of the DMSO-HBr adducts assists hole transport in OTFTs. Besides, we notice that adding a large amount of the adducts [i.e. DMSO-HBr (H) in Fig. 5d], despite the fact that the adduct doping effect still exists (i.e. improving the amount of hole current conveyed), can cause an adverse effect (e.g. acting as a scattering centre) as commonly observed in other doping schemes.[28] As such, the deteriorate electrical characteristics obtained from the DMSO-HBr (H) device could reflect the effective incorporation of the adduct dopants. To verify our hypothesis, we further fabricated the C_{16} IDT-BT OTFTs using the same device architecture with low work-function Al electrodes for the injection of electrons. The electrical characteristics obtained from the pristine, DMSO-HBr (M) and DMSO-HBr (H) devices are shown in Supplementary Figure 33. We found that the electron transport is largely supressed by adding the DMSO-HBr adducts. Furthermore, a larger amount of the adducts can induce severe detrimental effects in the OTFT electrical characteristics, e.g. lower electron current and larger hysteresis. This observation well corroborates our point on the effective p-doping scheme for the p-type OTFTs. We further fabricate OTFT using undoped and moderately- and heavily-doped C_{16} IDT-BT based on the solution-processed DMSO-HBr-CSA adduct doping approach. The devices doped with DMSO-HBr-CSA shows the same electronic property tendency with the DMSO-HBr doped devices. In Supplementary Table 4, we summarise performance parameters from the transfer characteristics in Supplementary Figure 34.

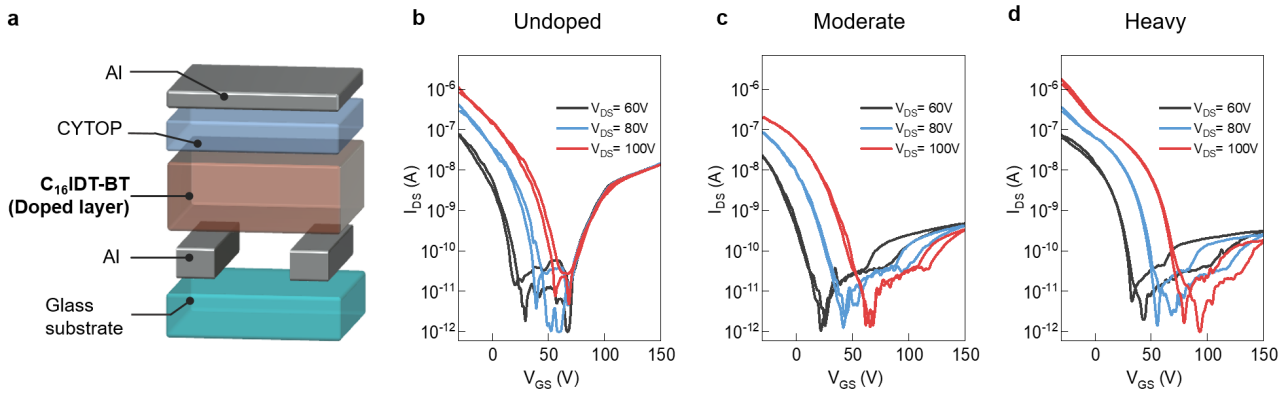

Supplementary Figure 33 | C_{16} IDT-BT OTFT n-type transfer characteristics. Schematic of the organic thin film transistor (OTFT) with Al contact on source and drain. Transfer current-voltage characteristics measured for TG-BC C_{16} IDT-BT OTFTs with different DMSO-HBr adduct doping levels.

Supplementary Table 3 | C_{16} IDT-BT OTFT performance parameters. Summary of key performance parameters obtained from pristine, DMSO-HBr (M) and DMSO-HBr (H) OTFTs shown in Fig. 5d. μ_{sat}, V_{TH}, On/Off, SS, ΔN_{tr} and D_{tr} denote saturation field-effect mobility, threshold voltage, current on-off ratio, subthreshold swing, areal trap density and trap concentration per unit energy, respectively.

Doping	Mobility (μ_{sat}) ($cm^2 V^{-1} s^{-1}$)	V_{TH} (V)	On/Off	SS (V/dec)	Areal trap density (ΔN_{tr}) (cm^{-2})	Trap concentration per unit energy (D_{tr}) ($eV^{-1} cm^{-2}$)
Pristine	0.14	-38.36	7.68×10^4	-5.25	-	1.14×10^{12}
Moderate	1.72	-12.69	2.72×10^4	-3.96	3.36×10^{11}	0.86×10^{12}
Heavy	0.37	-19.11	0.13×10^4	-11.62	2.52×10^{11}	2.54×10^{12}

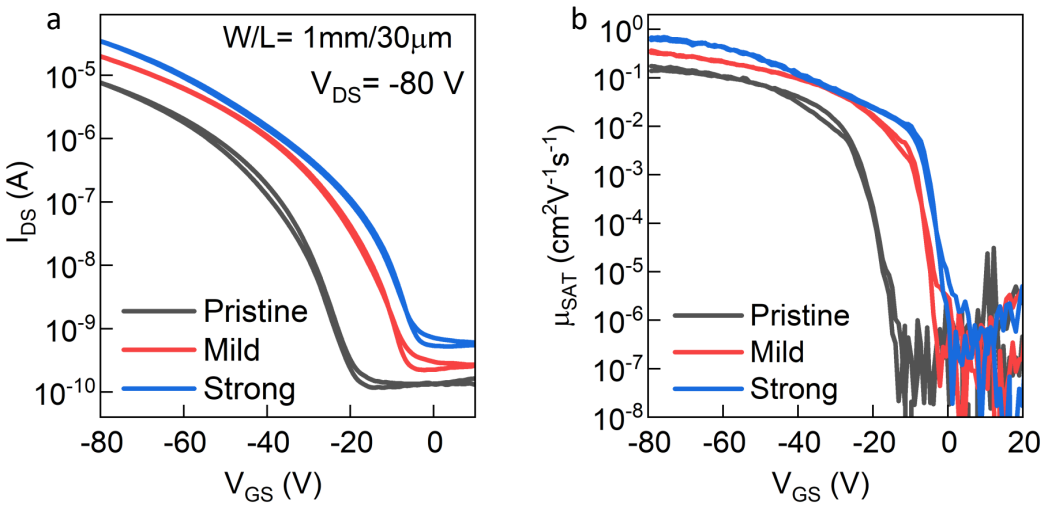

Supplementary Figure 34 | Current-voltage characteristics of DMSO-HBr-CSA doped C_{16} IDT-BT OTFT. Transfer characteristics obtained from OTFTs fabricated using pristine and moderately- [DMSO-HBr-CSA (M)] and heavily-doped [DMSO-HBr-CSA (H)] C16 IDT-BT based on the adduct doping approach.

Supplementary Table 4 | C_{16} IDT-BT OTFT performance parameters. Summary of key performance parameters obtained from pristine, DMSO-HBr-CSA (M) and DMSO-HBr-CSA (H) OTFTs shown in Supplementary Figure 34 μ_{sat}, V_{TH}, On/Off, Subthreshold slope (SS), ΔN_{tr} and D_{tr} denote saturation field-effect mobility, threshold voltage, current on-off ratio, subthreshold swing, areal trap density and trap concentration per unit energy, respectively.

Doping	Mobility (μ_{sat}) ($cm^2 V^{-1} s^{-1}$)	V_{TH} (V)	On/Off	SS (V/dec)	Areal trap density (ΔN_{tr}) (cm^{-2})	Trap concentration per unit energy (D_{tr}) ($eV^{-1} cm^{-2}$)
Pristine	0.14	-38.36	7.68×10^4	-5.25	-	1.14×10^{12}
Moderate	0.24	-32.87	9.04×10^4	-4.6	7.20×10^{10}	1.02×10^{12}
Heavy	0.37	-35.83	6.63×10^4	-5.93	3.32×10^{10}	1.32×10^{12}

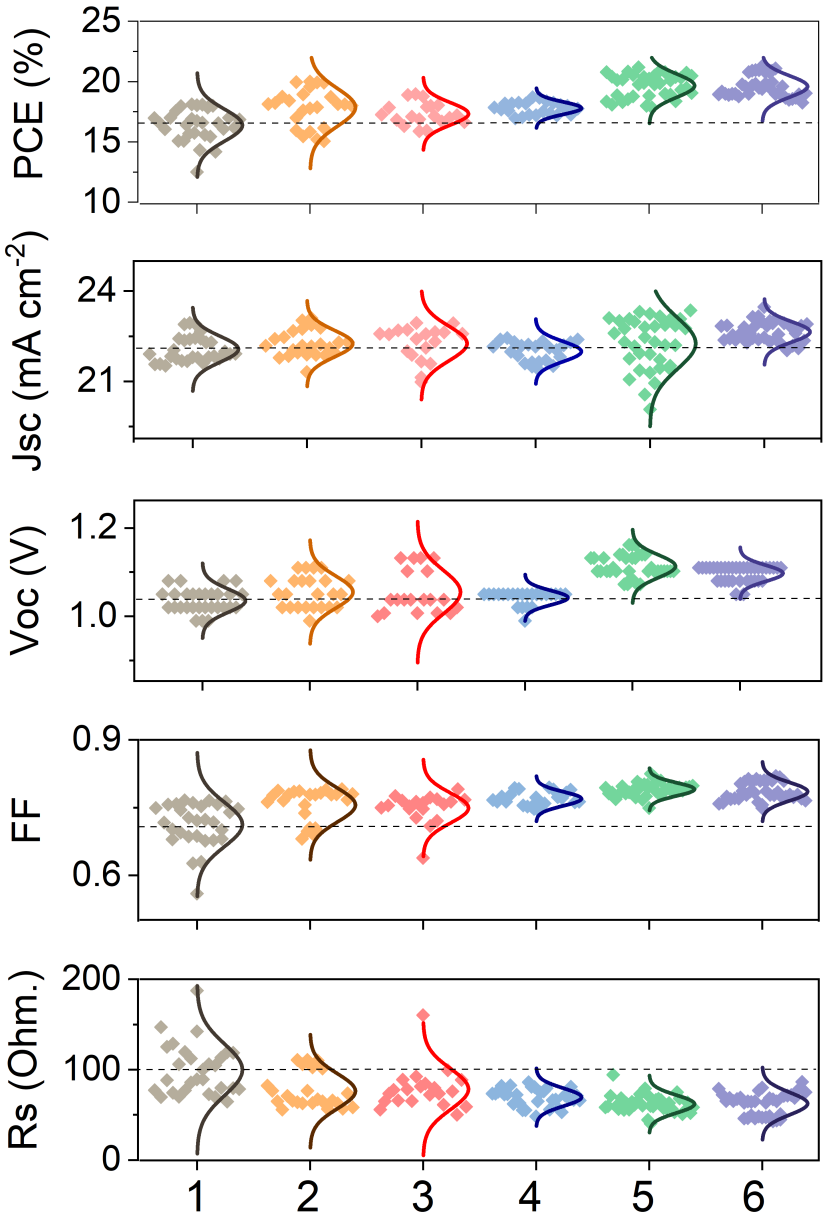

Supplementary Figure 35 | Performance parameters of the perovskite solar cells with doped Spiro-OMeTAD layer prepared with different doping methods. The performance parameters are extracted from forward bias to short-circuit. **1** : doping by Li-TFSI-oxygen in air for 12-15 hrs, **2**: doping by Co[III]TFSI-Li-TFSI-oxygen, **3**: doping by DMSO-HBr in a solution process, **4**: doping with DMSO-HBr by the vapor process (exposure time = 30 sec), **5**: doping with DMSO-HBr by solution process followed by a vapour process (exposure time = 30 sec), and **6**: doping with DMSO-HBr-CSA in a solution process.

Supplementary Table 5 | Device performance parameters of the perovskite solar cells with doped Spiro-OMeTAD layer prepared with different doping methods. The performance parameters for Jsc, Voc, FF, and PCE are extracted from forward bias to short-circuit. The data for J_{SC}, V_{OC}, FF, Rs and PCE are represented as an average value and the standard deviation (n>20). The data for J_{MPP} and SPO are represented as an average value and the standard deviation (n>8).

Doping method	n	J_{SC} (mA cm^{-2})	V_{OC} (V)	FF	PCE (%)	Rs (Ω)	J_{MPP} (mA cm^{-2})	SPO (%)
Li-TFSI-Oxygen	29	22.1 ± 0.43	1.04 ± 0.03	0.71 ± 0.05	16.4 ± 1.32	99.9 ± 28.6	19.4 ± 1.04	16.3 ± 0.60
Co(III)complex	24	22.2 ± 0.44	1.06 ± 0.04	0.76 ± 0.03	17.8 ± 1.52	76.2 ± 19.3	19.5 ± 1.24	17.1 ± 2.07
DMSO-HBr (Solution process)	21	22.3 ± 0.57	1.05 ± 0.05	0.75 ± 0.03	17.3 ± 1.52	78.5 ± 22.6	20.0 ± 0.85	16.4 ± 0.33
DMSO-HBr (Vapour process)	33	21.9 ± 0.40	1.06 ± 0.04	0.77 ± 0.01	18.1 ± 0.71	69.5 ± 9.83	18.7 ± 1.08	17.0 ± 0.58
DMSO-HBr (Solution+ Vapour process)	36	22.3 ± 0.85	1.11 ± 0.03	0.79 ± 0.01	19.7 ± 1.52	62.0 ± 9.77	19.8 ± 1.14	18.9 ± 0.79
DMSO-HBr-CSA (Solution process)	36	22.6 ± 0.34	1.10 ± 0.02	0.79 ± 0.02	19.6 ± 0.88	62.5 ± 12.4	20.4 ± 0.32	18.8 ± 0.81

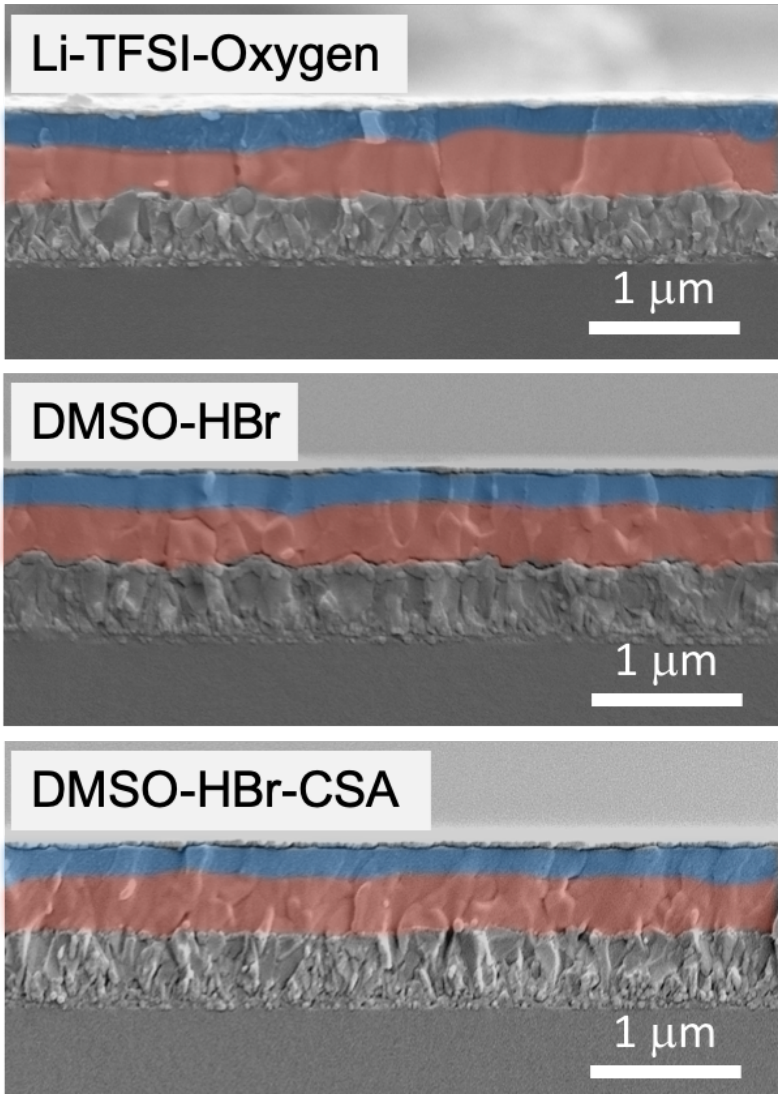

Supplementary Figure 36| Cross-section SEM images of the perovskite solar cell stack. The Spiro-OMeTAD layer (pseudo-color blue) doped with Li-TFSI-Oxygen, DMSO-HBr, and DMSO-HBr-CSA on top of perovskite (pseudo-color red). The device configuration is FTO (~500 nm) glass/SnO_2 CL (~50 nm)/$FA_{0.83}Cs_{0.17}Pb(I_{0.85}Br_{0.15})_3$ (~400 nm)/Spiro-OMeTAD (~200 nm)/Au (~50 nm).

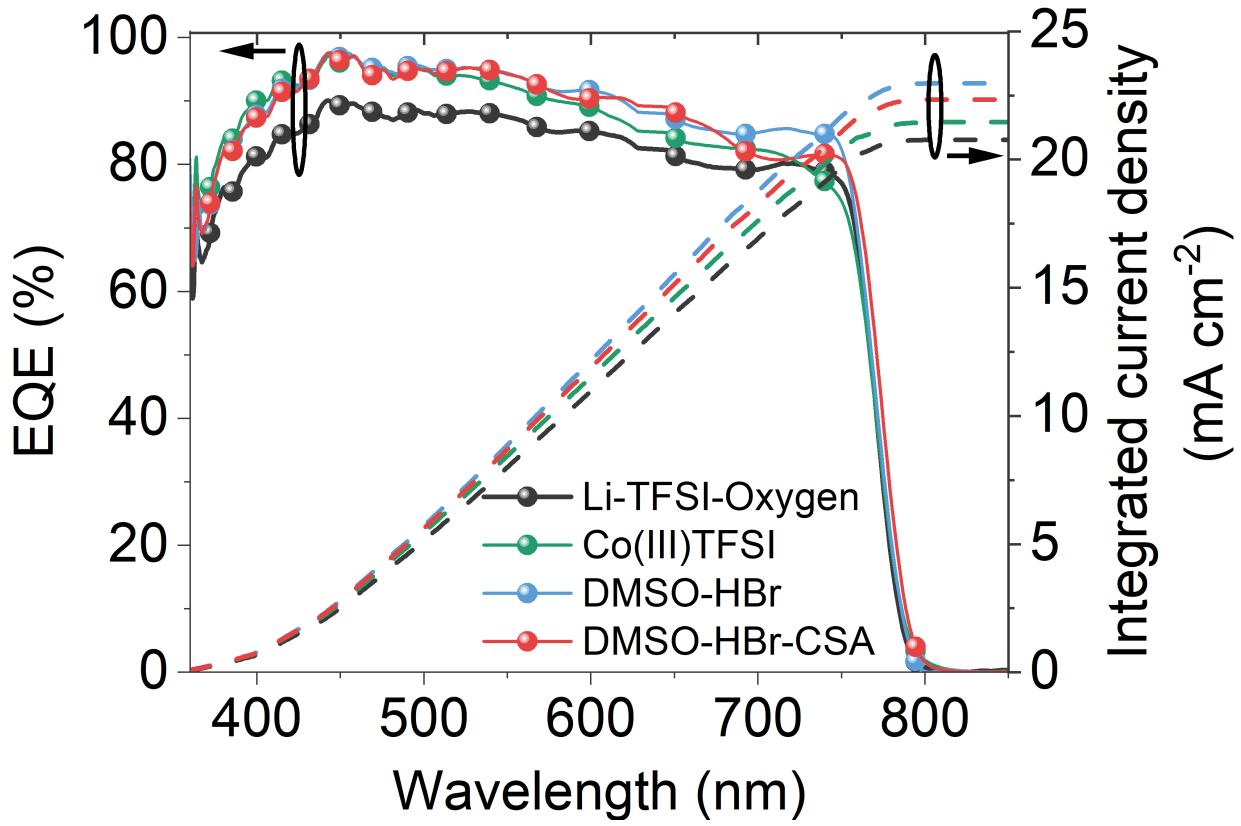

Supplementary Figure 37 | External quantum efficiency (EQE) of the perovskite solar cells. The Spiro-OMeTAD thin film doped by different doping methods.
On increased short circuit current due to doping:

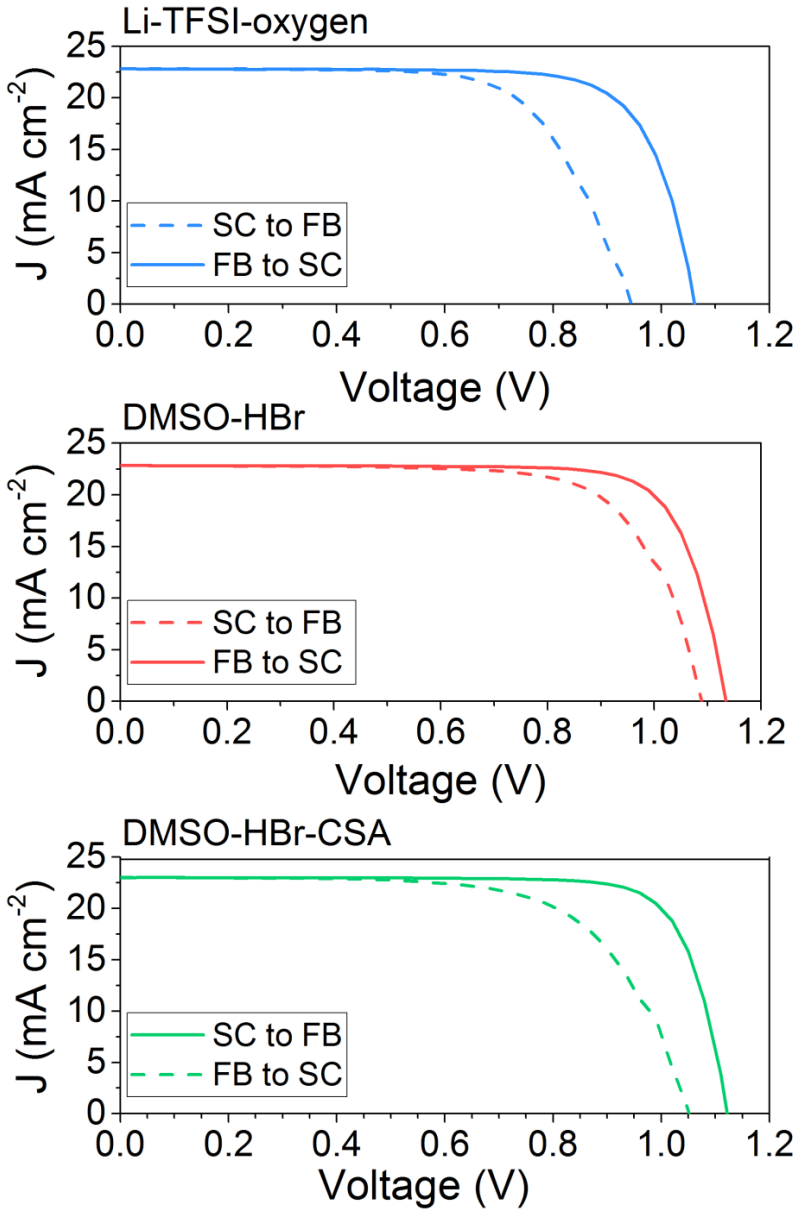

Supplementary Figure 38| Hysteresis property of the perovskite solar cell. Both forward-bias to short-circuit (FB-SC) and short-circuit to forward-bias (SC-FB) current density-voltage sweeps of the devices with different doping methods used to doped Spiro-OMeTAD films, the HTM layer in the solar cell. JV curve hysteresis still persists for all devices. However, the perovskite solar cell with doped Spiro-OMeTAD with DMSO-HBr and DMSO-HBr-CSA exhibit a reduction in hysteresis.

Supplementary Table 6 | Device performance parameters for both forward-bias to short-circuit (FB-SC) and short-circuit to forward-bias (SC-FB) current density-voltage sweeps. Devices use Spiro-OMeTAD films, the HTM layer in the solar cells, doped by different doping methods.

Doping method	Sweeps	J_{SC} (mA cm^{-2})	V_{OC} (V)	FF (%)	PCE (%)
Li-TFSI-oxygen	FB → SC	22.8	1.05	77.2	18.4
	SC → FB	22.8	0.93	69.2	14.6
DMSO-HBr	FB → SC	22.8	1.14	78.6	20.6
	SC → FB	22.8	1.08	72.9	18.1
DMSO-HBr-CSA	FB → SC	23.0	1.11	80.9	20.8
	SC → FB	23.0	1.05	66.8	16.3

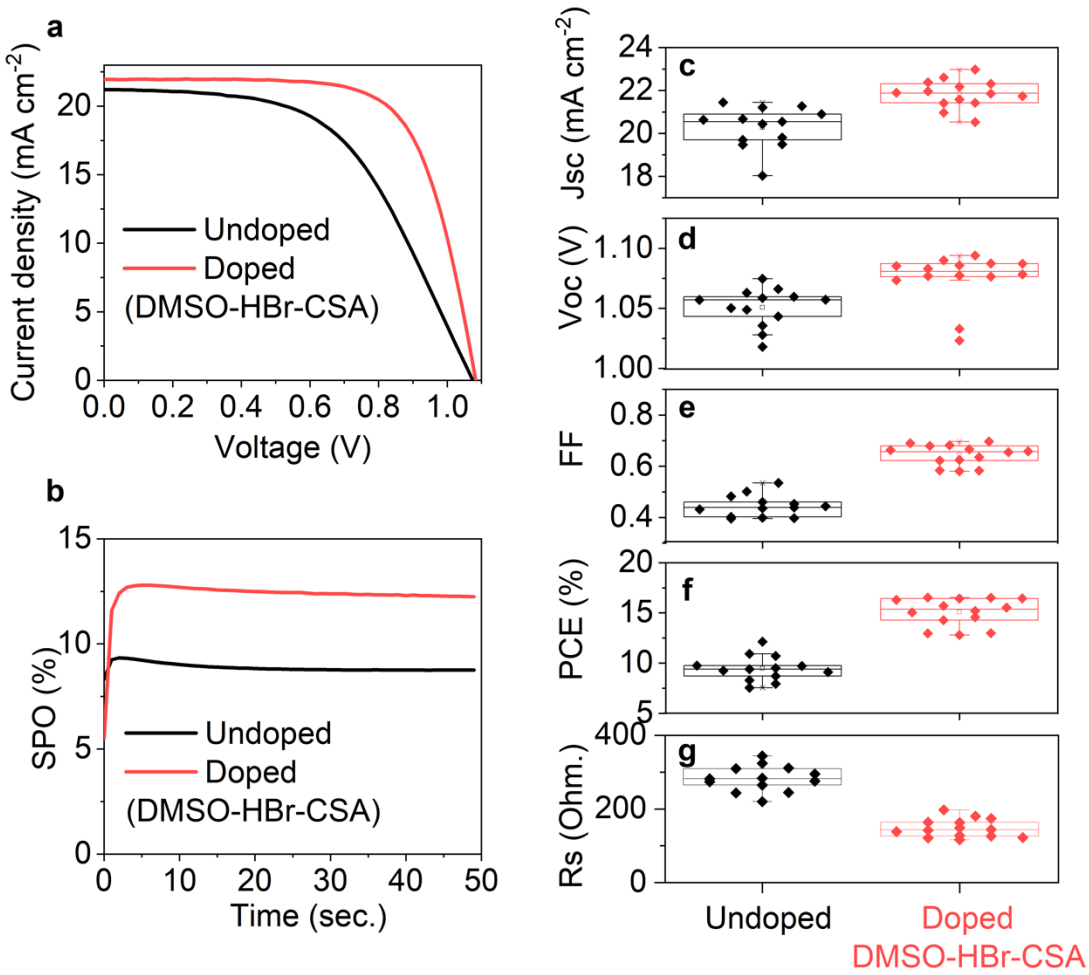

Supplementary Figure 39 | PV performances and performance parameters of the perovskite solar cells with doped Poly[bis(4-phenyl)(2,4,6-trimethylphenyl)amine (PTAA) layer prepared with different doping methods. **a** J-V curves for perovskite solar cells with the undoped HTM and doped with DMSO-HBr-CSA. The configuration of devices is FTO/SnO_2/$FA_{0.83}Cs_{0.17}Pb(I_{0.85}Br_{0.15})_3$/PTAA (without extra additives, Li-TFSI and tBP)/Au. **b** Steady-state power output (SPO) for the respective perovskite solar cells at the fixed maximum power point voltage. **c-g** The data are represented as a standard boxplot where the box range is defined by the standard deviation (n>15). Ninety percent of all data points fall within the upper and lower whisker. These measurements were carried under simulated sun light (99.2 $mWcm^{-2}$, AM1.5)

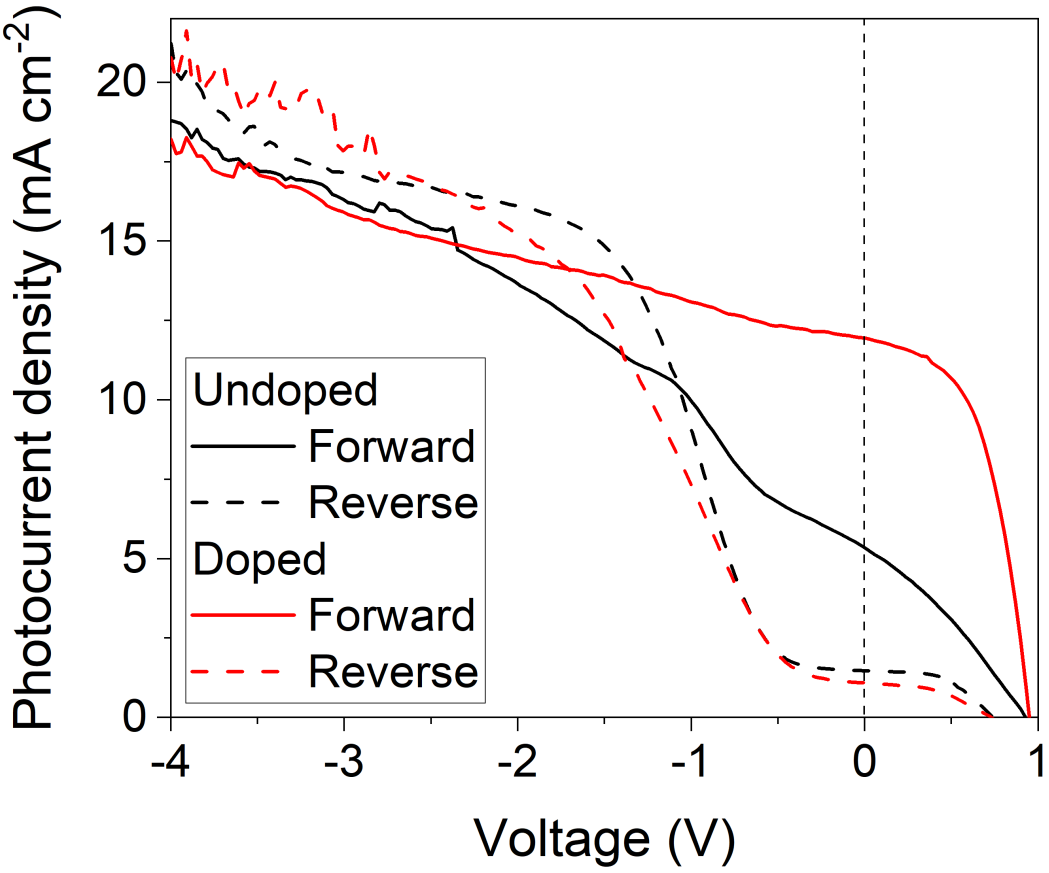

Supplementary Figure 40 | Both forward (Positive bias to negative bias) and reverse (negative bias to positive bias) current density-voltage sweeps of the perovskite solar cells with undoped and doped Spiro-OMeTAD as HTM. The configuration of devices is FTO/SnO_2/$FA_{0.83}Cs_{0.17}Pb(I_{0.85}Br_{0.15})_3$/Spiro-OMeTAD (with or without dopant additives Li-TFSI and tBP)/Au. These measurements were carried under simulated sun light (99.2 mW/cm^2), AM1.5). We note that massive hysteresis is induced in the reverse JV scan, due to scanning to and from -4V in reverse bias. This has been previously observed.[29]

Supplementary Note 9: *On increased short circuit current due to doping:*

We have provided justifications as to why the FF and open-circuit voltage improve with our adduct-based doping strategy. However, the increase in J_{SC} is less intuitive. There are many examples in the literature of perovskite solar cells, where increased J_{SC} is observed with increased doping of the HTM[30–33]. This is most clearly illustrated by showing the JV curves for a perovskite solar cell with spiro-OMeTAD and no doping of the HTM, as we show in Supplementary Fig. 40. In this instance, the J_{SC} is approximately half the value of J_{SC} in the device with the doped HTM. However, upon applying a 2.5V reverse bias, the photocurrents of the doped and non-doped devices coincide. If this short-circuit current density was solely limited by series resistance, we expect the JV curve to be a straight line from open-circuit to short-circuit. However, there remains some curvature in the JV curve of the un-doped device, indicating that this is not simply a series resistance limitation. This therefore illustrates that doping of the HTM does influence charge extraction under all working conditions, including short-circuit. Without doping, an external applied electric field appears to be required in order to extract all photogenerated carriers. This indicates a charge extraction barrier being present with the undoped HTM.

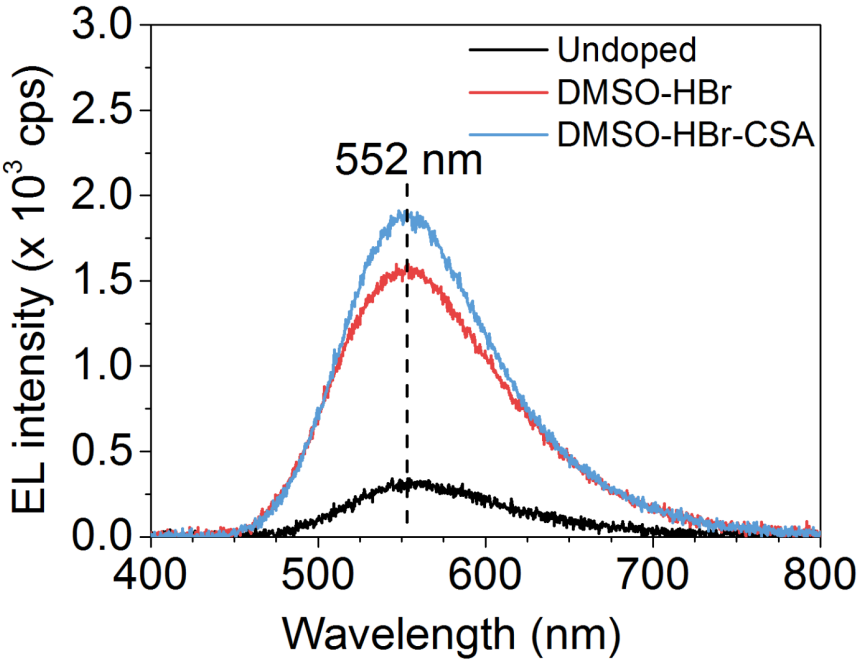

Supplementary Figure 41 | EL spectra of OLEDs. Steady-state electroluminescence (at 18 V) of the organic light emitting diodes.

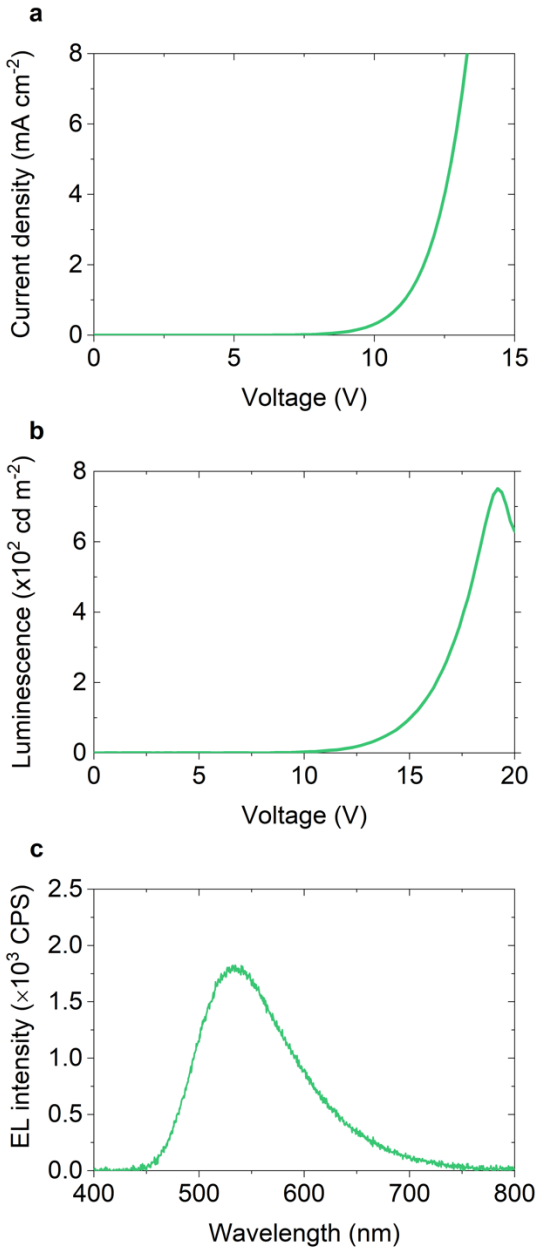

Supplementary Figure 42 | Electronic and luminescence performances of OLED doped with F4TCNQ. a, Current density-voltage curve of the OLED. b, luminescence-voltage curve for the OLED with F4TCNQ as dopant, c, Steady-state electroluminescence of the OLED biased at 19V.

References

1. Schroeder, P. G., France, C. B., Parkinson, B. A. & Schlaf, R. Orbital alignment at p-sexiphenyl and coronene/layered materials interfaces measured with photoemission spectroscopy. *J. Appl. Phys.* **91**, 9095–9107 (2002).

2. Poczatek, C., Kaufman, Z. & Lechene, C. OpenMIMS ImageJ Plugin Guide Opening MIMS images. *Harvard Med. Sch. (Boston, Massachusetts, USA)* (2009).

3. Kirchartz, T. *et al.* Sensitivity of the Mott − Schottky Analysis in Organic Solar Cells. *J. Phys. Chem. C* **116**, 7672–7680 (2012).

4. Deledalle, F. *et al.* Understanding the Effect of Unintentional Doping on Transport Optimization and Analysis in Efficient Organic Bulk-Heterojunction Solar Cells. *Phys. Rev. X* **5**, 11032 (2015).

5. Zonno, I., Martinez-Otero, A., Hebig, J. & Kirchartz, T. Understanding Mott-Schottky Measurements under Illumination in Organic Bulk Heterojunction Solar Cells. *Phys. Rev. Appl.* **7**, 034018 (2017).

6. Sherkar, T. S., Momblona, C., Gil-Escrig, L., Bolink, H. J. & Koster, L. J. A. Improving Perovskite Solar Cells: Insights From a Validated Device Model. *Adv. Energy Mater.* **7**, 1602432 (2017).

7. Schroder, D. K. Semiconductor Material and Device Characterization. *John Wiley & Sons, Inc.* (2005). doi:10.1002/0471749095

8. Green, M. A. Accuracy of analytical expressions for solar cell fill factors. *Sol. Cells* **7**, 337–340 (1982).

9. Ono, L. K. *et al.* Air-exposure-induced gas-molecule incorporation into spiro-MeOTAD films. *J. Phys. Chem. Lett.* **5**, 1374–1379 (2014).

10. Li, Z. *et al.* Acid Additives Enhancing the Conductivity of Spiro-OMeTAD Toward High-Efficiency and Hysteresis-Less Planar Perovskite Solar Cells. *Adv. Energy Mater.* **7**, 1–8 (2017).

11. Gratia, P. *et al.* A Methoxydiphenylamine-Substituted Carbazole Twin Derivative: An Efficient Hole-Transporting Material for Perovskite Solar Cells. *Angew. Chemie - Int. Ed.* **54**, 11409–11413 (2015).

12. Fehse, K. *et al.* Energy level alignment of electrically doped hole transport layers with transparent and conductive indium tin oxide and polymer anodes. *J. Appl. Phys.* **102**, 1–5 (2007).

13. Tietze, M. L., Burtone, L., Riede, M., Lüssem, B. & Leo, K. Fermi level shift and doping efficiency in p -doped small molecule organic semiconductors : A photoelectron spectroscopy and theoretical study. *Phys. Rev. B* **035320**, 1–12 (2012).

14. Olthof, S., Tress, W., Meerheim, R., Lüssem, B. & Leo, K. Photoelectron spectroscopy study of systematically varied doping concentrations in an organic semiconductor layer using a molecular p-dopant. *J. Appl. Phys.* **106**, (2009).

15. Méndez, H. *et al.* Charge-transfer crystallites as molecular electrical dopants. *Nat. Commun.* **6**, (2015).

16. Kim, J. B. *et al.* Small-molecule thiophene-C60 dyads as compatibilizers in inverted polymer solar cells. *Chem. Mater.* **22**, 5762–5773 (2010).

17. Intaniwet, A., Mills, C. A., Sellin, P. J., Shkunov, M. & Keddie, J. L. Achieving a stable time response in polymeric radiation sensors under charge injection by X-rays. *ACS Appl. Mater. Interfaces* **2**, 1692–1699 (2010).

18. Endres, J. *et al.* Electronic structure of the CsPbBr 3 /polytriarylamine (PTAA) system. *J. Appl. Phys.* **121**, 1–8 (2017).

19. Sun, Q. *et al.* Bright, multicoloured light-emitting diodes based on quantum dots. *Nat. Photonics* **1**, 717–722 (2007).

20. Kim, D. H. & Kim, T. W. Enhancement of the current efficiency of organic light-emitting devices due to the surface plasmonic resonance effect of dodecanethilol-functionalized Au nanoparticles. *Org. Electron. physics, Mater. Appl.* **34**, 262–266 (2016).

21. Ki Bae, W. *et al.* Deep blue light-emitting diodes based on $Cd_{1-x}Zn_xS$ @ ZnS quantum dots. *Nanotechnology* **20**, 075202 (2009).

22. Son, D. I., Kim, H. H., Hwang, D. K., Kwon, S. & Choi, W. K. Inverted CdSe–ZnS quantum dots light-emitting diode using low-work function organic material polyethylenimine ethoxylated. *J. Mater. Chem. C* **2**, 510–514 (2014).

23. Wan, A., Hwang, J., Amy, F. & Kahn, A. Impact of electrode contamination on the α-NPD/Au hole injection barrier. *Org. Electron.* **6**, 47–54 (2005).

24. Fujiwara, H. Spectroscopic Ellipsometry: Principles and Applications. *John Wiley & Sons, Ltd* (2007). doi:doi:10.1002/9780470060193.fmatter

25. Christians, J. A. *et al.* Tailored interfaces of unencapsulated perovskite solar cells for >1,000 hour operational stability. *Nat. Energy* **3**, 68–74 (2018).

26. Leijtens, T. *et al.* Hydrophobic Organic Hole Transporters for Improved Moisture Resistance in Metal Halide Perovskite Solar Cells. *ACS Appl. Mater. Interfaces* **8**, 5981–5989 (2016).

27. Zhang, X. *et al.* Molecular origin of high field-effect mobility in an indacenodithiophene–benzothiadiazole copolymer. *Nat. Commun.* **4**, 2238 (2013).

28. Panidi, J. *et al.* Remarkable Enhancement of the Hole Mobility in Several Organic Small-Molecules, Polymers, and Small-Molecule:Polymer Blend Transistors by Simple Admixing of the Lewis Acid p-Dopant B(C6F5)3. *Adv. Sci.* **5**, 1700290 (2018).

29. Zhang, Y. *et al.* Charge selective contacts, mobile ions and anomalous hysteresis in organic–inorganic perovskite solar cells. *Mater. Horizons* **2**, 315–322 (2015).

30. Nguyen, W. H., Bailie, C. D., Unger, E. L. & McGehee, M. D. Enhancing the Hole-Conductivity of Spiro-OMeTAD without Oxygen or Lithium Salts by Using Spiro(TFSI)2 in Perovskite and Dye-Sensitized Solar Cells. *J. Am. Chem. Soc.* **136**, 10996–11001 (2014).

31. Xi, H. *et al.* Performance Enhancement of Planar Heterojunction Perovskite Solar Cells through Tuning the Doping Properties of Hole-Transporting Materials. *ACS Omega* **2**, 326–336 (2017).

32. Wong-Stringer, M. *et al.* Efficient perovskite photovoltaic devices using chemically doped PCDTBT as a hole-transport material. *J. Mater. Chem. A* **5**, 15714–15723 (2017).

33. Ulfa, M., Pauporté, T., Bui, T.-T. & Goubard, F. Impact of Organic Hole Transporting Material and Doping on the Electrical Response of Perovskite Solar Cells. *J. Phys. Chem. C* **122**, 11651–11658 (2018).